Geothermics 127 (2025) 103253

Contents lists available at ScienceDirect

Geothermics

journal homepage: www.elsevier.com/locate/geothermics

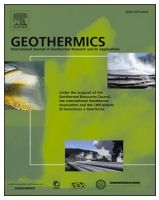

Contemporary crustal stress in the Guangdong-Hong Kong-Macao Greater Bay Area, SE China: Implications for geothermal resource exploration and seismic hazard assessment

Xianrui Li [a,b,*], Shaopeng Huang [b,*], Tobias Hergert [c], Andreas Henk [d], Danhua Xin [e,f]

[a] Guangdong Laboratory of Artificial Intelligence and Digital Economy (SZ), 518107 Shenzhen, China
[b] Institute of Advance Study, Shenzhen University, 518060 Shenzhen, China
[c] Institute of Applied Geosciences, Karlsruhe Institute of Technology, 76131 Karlsruhe, Germany
[d] Institute of Applied Geosciences, Technical University of Darmstadt, 64287 Darmstadt, Germany
[e] Department of Earth and Space Sciences, Southern University of Science and Technology, 518055 Shenzhen, China
[f] Key Laboratory of Earthquake Forecasting and Risk Assessment, Ministry of Emergency Management, Southern University of Science and Technology, 518055 Shenzhen, China

ARTICLE INFO

Keywords:
3D geomechanical model
Structure permeability
Focal mechanism solution
Reservoir-induced earthquake
Slip and dilation tendency
Geothermal resource

ABSTRACT

Geothermal resources and seismic activity are two related earth science frontiers that are of great significance to socioeconomic development. The Guangdong-Hong Kong-Macao Greater Bay Area (GBA) in southeastern China is a geothermal resource-rich and seismically active region. Crustal stress information is crucial for identifying prospective hidden geothermal fields and assessing seismic hazards. However, the characteristics of crustal stress in the GBA region remain unclear. In this study, we construct a high-resolution three-dimensional (3D) geomechanical model of the GBA region with complex fault geometries and obtain the 3D stress state. The results show that the GBA region is subject to a laterally variable crustal stress field. The maximum horizontal stress (S_H) is oriented predominantly NW-SE in the east of the study area and rotates to nearly N-S in the west. The shallow crust is dominated by a transpressional stress regime, while the deeper part exhibits transtension. Detailed stress analyses on typical individual faults show that the NW-trending faults commonly have low normal stresses and high dilation tendencies, thus favoring geothermal fluid circulation. In contrast, the ENE-/NE-trending faults, at high angles to the S_H orientation, tend to act as barriers to fluid flow in the shallow crust and accumulate high strain energy, making them conducive to the generation of strong earthquakes. We propose a comprehensive conceptual model to illustrate the genetic mechanism of geothermal resources and strong earthquakes. This study is intended to promote the exploration of geothermal resources and support the seismic hazard assessment in the GBA region.

1. Introduction

The crustal stress state is a key parameter in geodynamics (e.g., Heidbach et al., 2018; Henk and Nemčok, 2008) with a wide range of practical applications, including evaluating the stability of potential radioactive waste disposal sites (Hergert et al., 2015), assessing seismic hazards of active faults (Li et al., 2022a, 2022b), and developing geothermal resources (Jolie et al., 2015; Dávalos-Elizondo and Laó-Dávila, 2023). Especially in geothermal resource development, knowledge of the present-day crustal stress state plays an increasingly important role in locating, maintaining, and sustainably developing these resources (Blake and Davatzes, 2011; Davatzes et al., 2006). By controlling the opening and closing of pre-existing fractures or faults within the rock, stress influences hydraulically relevant physical properties such as rock mass permeability (Evans et al., 1997), thereby controlling the fluid flow along faults, which is closely linked to the distribution of geothermal systems (Siler et al., 2019). Most geothermal fields operated worldwide typically require highly permeable fault systems, which are commonly governed by extensional or strike-slip regimes (Moeck, 2014). These fault systems provide pathways for the ascent of geothermal fluids from deep levels and promote the development of fluid circulation systems, facilitating higher production flow

* Corresponding authors.
E-mail addresses: lixianrui1988@126.com (X. Li), shaopeng@szu.edu.cn (S. Huang).

https://doi.org/10.1016/j.geothermics.2025.103253
Received 29 September 2024; Received in revised form 21 December 2024; Accepted 4 January 2025
Available online 15 January 2025

rates. Therefore, studying the crustal stress state can help identify favorable faults for the development of potential geothermal utilities (e.g., Jolie et al., 2016) and improve the understanding of the distribution and genetic mechanism of geothermal resources. Moreover, since crustal stress is closely related to earthquakes, stress information is also critical for assessing potential earthquakes that could occur during geothermal exploitation (Moein et al., 2023).

The Guangdong-Hong Kong-Macao Greater Bay Area (GBA) is an urban agglomeration in southern China, primarily comprising nine neighboring cities in Guangdong province, along with Hong Kong and Macao (Fig. 1). This region is characterized by high economic vitality and requires green energy to sustain its socioeconomic development in the context of global warming and China's 2030 carbon peak policy constraints. As an important member of the renewable energy family (Huang, 2012), geothermal resource is rich in the GBA region (Wei et al., 2024b) due to the widely distributed granitoids (Zhou et al., 2006) and relatively high geothermal heat flow (Jiang et al., 2019). The first geothermal power plant in China was constructed in 1970 in Fengshun County, near the eastern side of the GBA. However, geothermal energy development in the GBA has progressed very slowly since then. One important reason for this stagnation is the insufficiency of research on the geothermal-controlling structures in the region. Specifically, the limited knowledge on the crustal stress in this area makes it challenging to evaluate the stress state of geothermal fluid flow-controlling faults, which further affects the identification of potential geothermal systems and increases the risk of investment and development of geothermal energy extraction.

The primary reason for the limited knowledge on the crustal stress in the GBA region is the scarcity of stress meansurements. The updated World Stress Map (WSM) released in 2016 compiled 42,870 global records, providing information on the orientation of the maximum horizontal stress (S_H) and the stress regime (Heidbach et al., 2018). However, only nine relatively reliable (B-/C-Quality) stress records exist in the GBA, many of which are from shallow depths and lack magnitude information (Fig. 1). A few in-situ stress measurements have been conducted in recent years. For instance, to evaluate the stability of faults near nuclear power plants in the region, Feng et al. (2013) used the hydraulic fracturing method to acquire stress characteristics at nuclear power plants in Dayawan, Taishan, and Yangjiang (see Fig. 1). They found that S_H is oriented NW-SE to WNW-ESE in Dayawan and Yangjiang, changing to NNW-SSE in Taishan. In-situ stress measurements conducted in wells in the Huangshadong geothermal field, located in the eastern part of the study area, indicate that the orientation of S_H is WNW-ESE at depths ranging from hundreds of meters to 3 km (Fan et al., 2022; Zhang et al., 2023). Lai et al. (2019) reviewed previous in-situ stress test results and confirmed that the Hong Kong area is generally

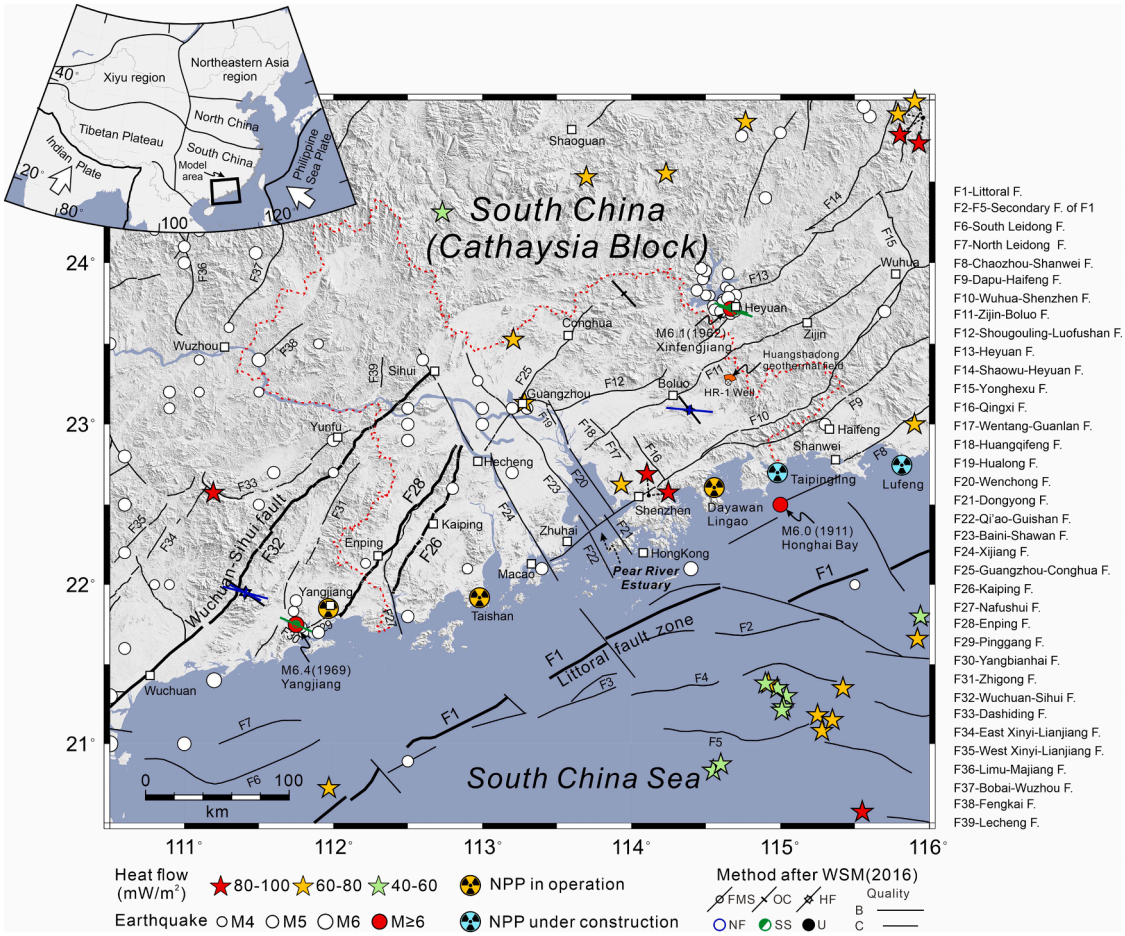

Fig. 1. Map showing faults, earthquakes, heat flow measurements, and stress data records in the Guangdong-Hong Kong-Macao Greater Bay Area (GBA) and surrounding areas. Black lines represent faults; Red and white circles indicate earthquakes of $M \geq 6.0$ and $M \geq 4.0$, respectively; Colored stars represent heat flow measurements with different values (from the International Heat Flow Commission and Tang et al., 2014); Colored bars with different symbols show the S_H orientations of quality B–C from the World Stress Map (WSM) obtained by different methods: FMS-Focal Mechanism Single, OC-Overcoring, HF-Hydraulic Fracturing, NF-Normal faulting regime, SS-Strike-slip faulting regime, U-Unknown faulting regime (Heidbach et al., 2018); Brown and ice blue radiation symbols indicate Nuclear Power Plants (NPP) in operation and under construction, respectively; The small orange polygon in the south of F11 represents the location of the Huangshadong geothermal field; The red dotted line is the administrative boundary of the GBA. The inset shows the tectonic setting, with a black box indicating the location of Fig. 1 and the model region.

dominated by WNW-ESE compression. Unlike in-situ stress measurements, which are typically limited to shallow depths up to a few kilometers, earthquake focal mechanism solutions (FMS) can reveal the stress state in the deep crust. P-axes inverted from FMSs in the GBA are mainly oriented NW-SE (Kang et al., 2008). Although these studies provide a basic understanding of GBA's crustal stress state, obtaining detailed stress characteristics for specific faults in this region remains challenging due to the sparse and incomplete nature of these pointwise stress data, which primarilly provides information on S_H orientation but offer limited constraints on the magnitudes of the three principal stresses.

One (and possibly the only) way to obtain a spatially continuous stress field description is by geomechanical-numerical modeling. Several successful studies have been conducted on absolute crustal stress at scales ranging from tens to thousands of kilometers in regions such as Türkiye (Hergert and Heidbach, 2011), Canada (Reiter and Heidbach, 2014), Switzerland (Hergert et al., 2015), Germany (Ahlers et al., 2021, 2022), and China (Li et al., 2022a, 2022b). A common approach in these studies is to incorporate an appropriate initial stress state into the model as well as a complex three-dimensional (3D) subsurface structure and an inhomogeneous rock property distribution and apply boundary conditions that account for the far field forces acting on the region, to predict the absolute stress state in the crust honoring the specific local conditions. However, there has been no such geomechanical modeling approach focusing on the absolute stress state in the GBA, except for a few two-dimensional (2D) models without consideration of faults (Wen et al., 2001; Chen et al., 2014) or 3D models with oversimplified faults (Dong et al., 2021).

In this study, we establish a comprehensive 3D geomechanical model of the GBA region which incorporates complex fault geometries, inhomogeneous rock properties, an initial stress state accounting for gravity, and appropriate boundary conditions. The model not only matches kinematic observations well (see Li et al., 2024b), but also predicts the spatially continuous 3D crustal stress state in the GBA region, thus it can address the limitations of sparse existing stress meansurements and enhancing our understanding of crustal stress state in the region. The kinematic characteristics of the crust revealed by the 3D geomechanical model has been described in detail in Li et al. (2024b). The present paper focuses specifically on the characteristics of the crustal stress field derived from the same geomechanical model. Modeled stress states at different depths are extracted and compared with various independent stress measurements, including S_H orientations and FMSs, to assess the model's accuracy. The stress states on major faults are also analyzed. Finally, the implications of the modeled stresses for geothermal resources and seismic hazard assessment of the faults within the GBA region are discussed.

2. Geological background

Tectonically, the GBA is situated on the southern edge of the South China Block, which consists of the Yangtze Block, the Jiangnan Orogenic Belt, and the Cathaysia Block from NW to SE. The South China Block is inferred to have initially formed in the middle Neoproterozoic and experienced multiple tectono-magmatic events during the Phanerozoic, eventually leading to the formation of extensive granitic rocks within the block (Shu et al., 2021). The Late Mesozoic igneous rocks (also known as Yanshanian granitoids) are the most widespread, especially in the Cathaysia Block. The age of the granite gradually becomes younger from inland to oceanic regions, a pattern commonly attributed to the paleo-Pacific Plate's northwestward subduction and the subsequent slab rollback (Zhou and Li, 2000; Zhou et al., 2006; Dong et al., 2020; Li et al., 2020).

Granite can generate heat through the decay of radioactive elements and is an important source of geothermal heat. In the GBA region, the widespread granite and a high mantle heat flow associated with a thinner crust (Lin et al., 2024) make the region rich in geothermal resources, as evidenced by numerous hot springs. The heat flow records within the GBA show an average heat flow value of 75.2 mW/m^2 (ihfc-iugg.org), which is noticeably higher than the average heat flow of continental China (60.4 mW/m^2) (Jiang et al., 2019). More than 106 hot springs are located in the GBA region (Li et al., 2024b). These hot springs primarily range in temperature from 25 to 118 °C and are closely related to faults. They are generally controlled by ENE-/NE-trending faults, but some clusters of hot springs are also found along NW-trending faults, which intersect the ENE-/NE-trending faults at high angles (Zhong and Zhou, 1990; Luo et al., 2022).

The faults within the study area can be categorized into three groups according to their strike: NE-trending, ENE-trending, and NW-trending (Fig. 1). Previous researchers often combined NE-trending and ENE-trending faults into a single group due to their similar strike (e.g., Wei, 2001, p. 60), but recent studies have revealed significant differences in the activity of these two faults groups, suggesting they should be treated separately (Yu et al., 2016). Our prior kinematic model results (Li et al., 2024b) together with field investigations (Huang and Zheng, 2001; Fan et al., 2022), also suggest different slip behaviors on the NE- and ENE-trending faults. The NE-trending faults show left-lateral movement, whereas the ENE-trending faults exhibit right-lateral motion. These opposite slip senses are believed to result from lateral variations in the crustal stress (see Section 4 for details). The NE- and ENE-trending faults are thought to have initially formed in the Triassic period and have experienced alternating stages of shortening and extension during the late Mesozoic due to the northwestward subduction of the paleo-Pacific Plate (Li et al., 2020). The NW-trending faults formed in the Late Cenozoic are the youngest of these three fault groups (Chan et al., 2010), cutting and reactivating the other two older fault groups.

The GBA region is located in the central part of the Southeast Coastal Seismic Zone, which runs roughly parallel to the coastline, extending 1500 km from Fujian Province in the north to Hainan Island in the south. Influenced by the westward motion of the Philippine Sea Plate, the seismic activity in the Southeast Coastal Seismic Zone is relatively high. Several large earthquakes with magnitudes above 7.0 have occurred in this seismic zone, including the 1600 Nan'ao *M*7.0 earthquake (117.2°E, 23.5°N), the 1604 Quanzhou *M*7.5 earthquake (119.2°E, 24.7°N), the 1605 Hainan *M*7.5 earthquake (110.5°E, 20.0°N), and the 1918 Nan'ao *M*7.3 earthquake (117.4°E, 23.3°N). Three strong earthquakes also occurred in the GBA region historically, i.e., the 1911 Honghai Bay *M*6.0 earthquake, the 1962 Xinfengjiang *M*6.1 earthquake, and the 1969 Yangjiang *M*6.4 earthquake (Wei, 2001) (Fig. 1). Shallow earthquake sources, along with thick sedimentary layers at the continental margin, make these earthquakes highly destructive, causing severe casualties and property damage in the region (Brantley and Chung, 1991; Wei, 2001, pp. 141, 154, 163). In 2023, an *M*3.2 earthquake in Foshan City and an *M*4.3 earthquake in Heyuan City occurred consecutively within one week, causing noticeable tremors in the mega-cities of Guangzhou and Shenzhen and capturing widespread media and public attention, despite their small magnitudes.

3. Model setup

In this study, we construct a high-resolution 3D geomechanical model of the GBA region and use finite element techniques to simulate the stress field. A detailed description of the model setup is provided in Li et al. (2024b); therefore, we present only key information about the modeling process here. The 3D geomechanical model covers the area from 110.5°E to 116°E and from 20.5°N to 25°N, spanning 572 km east-west and 490 km north-south (Fig. 2). The model's base is positioned at a depth of 38 km, slightly deeper than the maximum depth of the Moho discontinuity, which is 33 km (Guo et al., 2019). This design accounts for the potential influence of Moho topography on the crustal stress. The elevation of the ground surface of the model ranges from -0.6 km to 1.2 km, constrained by a digital elevation model with a 30

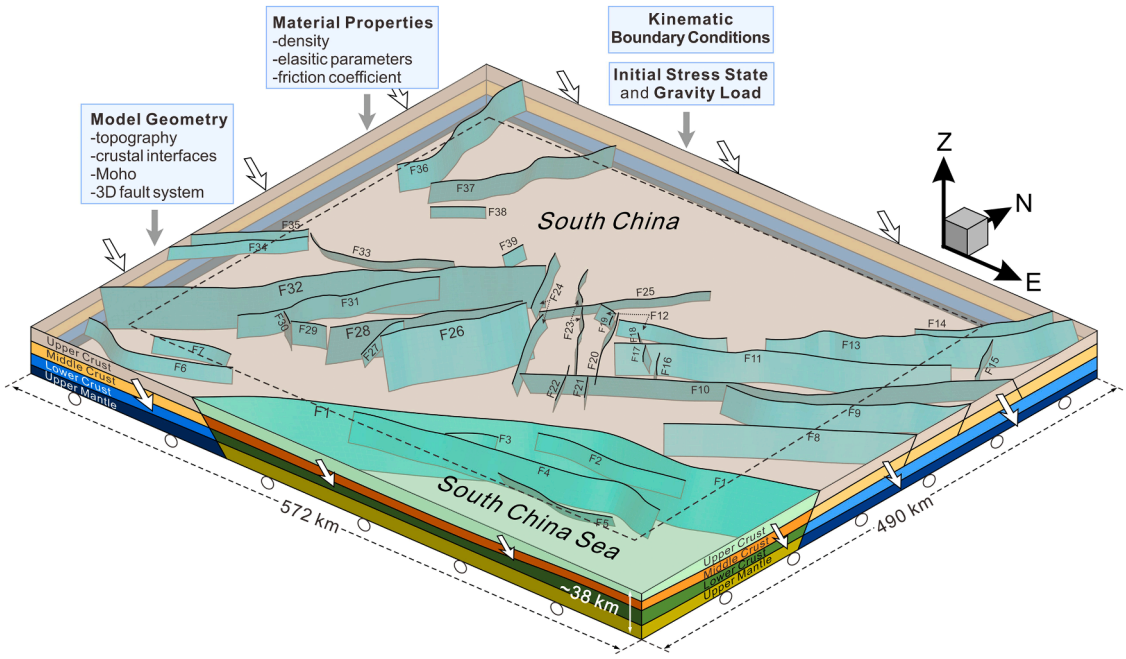

Fig. 2. 3D geomechanical model of the GBA region including the crust and the upper mantle, as well as a 3D fault system. The model size is 572 km (E-W) × 490 km (N-S) × 38 km (depth). Different rock properties are represented by different colors. The fault system consists of 39 faults reconstructed from multiple geoscience information sources. White arrows indicate the model boundary conditions with size and direction of arrows indicating amount and direction of velocities, respectively. White circles indicate frictionless constraints at the base of the model. Detailed model information is shown in the light blue boxes. The dashed box at the surface of the model, shrinking inward by 0.5 geographic degrees (about 50 km), delineates the presented area with marginal boundary effects. Fault numbers refer to Fig. 1.

arc-second (~1 km) resolution. Vertically, the model is divided into the upper, middle and lower crust, and the upper mantle, based on the Crust1.0 model (Laske et al., 2013). Fault geometries included in the model are compiled from various sources, including fault trace databases, deep seismic sounding profiles, FMSs, seismic tomography results and earthquake relocation data. These faults have variable depth extents, dip directions and dips (see Fig. 2). Detailed geometric parameters and data sources for the faults can be found in Li et al. (2024b).

The rock properties used in the model are based on the P- and S-wave velocities in Crust1.0, as outlined in Li et al. (2024b). These averaged values represent the general crustal properties of the region and are considered more reasonable than data derived from a single deep seismic sounding profile (e.g., Zhang et al., 2018; Lv et al., 2020), which may show different crustal velocity structures due to lateral heterogeneity. Fault motion within the model is governed by the Coulomb friction law, using an effective friction coefficient of 0.02. This low value minimizes the misfit between the model and kinematic observations (Li et al., 2024b) and is commonly used for large faults (He and Lu, 2007; Hergert and Heidbach, 2010; Li et al., 2021, 2022a). Clay-rich fault gouge is generally understood to promote a reduction in the effective friction coefficient (Lockner et al., 2011; Carpenter et al., 2015). For instance, the ultralow effective friction coefficient (<0.02) observed on the Longmen Shan fault (Li et al., 2015) is attributed to the abundance of clay minerals and graphite (Zhang and He, 2013; Kuo et al., 2014). Elevated pore fluid pressure can also effectively reduce the effective friction coefficient (Simpson and Reasenberg, 1994).

The current crustal stress field can be described as a superposition of the initial crustal stress and the tectonic stress states if the stress evolution caused by seismic cycles is not considered (Hergert and Heidbach, 2011). The initial crustal stress component includes a reference stress state (Sheorey, 1994) and stress perturbations resulting from lateral variations in rock density and stiffness (Hergert and Heidbach, 2011). The tectonic stress component, also known as far-field stress, originates from plate-driving forces (Zoback, 1992) and is integrated into our model by applying lateral velocity boundary conditions based on Global Position System (GPS) observations (Wang and Shen, 2020; Li et al., 2024b). A gravitational acceleration of 9.81 m/s^2 is applied to the model volume. The model bottom is vertically constrained, and the model top is a free surface. The load of the overlying water column in the South China Sea is neglected due to the relatively shallow water depth (<100 m) on the continental shelf.

Previous studies of FMSs (e.g. Kang et al., 2005a) suggest that the GBA region is predominantly characterized by a strike-slip faulting regime with a minor normal faulting component. To reproduce this stress state, the lateral tectonic stress should be set large enough to counteract the significant normal faulting stress regime resulting from the gravity-only initial stress state. In this study, we use velocity boundary conditions with a model time of 600 ka to simulate the effect of tectonic stress, which can best fit the kinematic observations (see Li et al., 2024b) and available stress data simultaneously.

The model is discretized into approximately 4 million linear tetrahedral elements. To balance computational efficiency and result accuracy, the element size on the faults is approximately 1–2 km, gradually increasing to around 5 km toward the model boundaries. We use the software SIMULIA Abaqus 2019 to perform the finite element calculations. For more detailed parameter settings related to the model setup and their rationale, the reader is referred to Li et al. (2024b), a complementary paper focusing primarily on crustal kinematic results in the GBA region. The stress field data presented here are extracted from the same model described in Li et al. (2024b).

4. Results

4.1. Stress state in the GBA region

The crustal stress state has a significant impact on rock, fracture and fault permeability, which further affects fluid flow in the rock mass. Hydrochemical analyses indicate that the maximum circulation depth of geothermal fluids in the GBA region is approximately 4 km (Yuan et al., 2022; Li et al., 2023; Tian et al., 2023; Wei et al., 2024c). Therefore, we

choose 2 km depth to represent the average depth of the geothermal fluid circulation and extract the stress state at this depth to investigate the potential relationship between stress and geothermal resources. Furthermore, given the close relationship between crustal stress and seismic hazard, we also extract the crustal stress state at 10 km depth, which represents the average depth of earthquake hypocenters in the area, as determined by earthquake relocation studies (He et al., 2018; Xia et al., 2022). The orientation of S_H is determined following the method of Lund and Townend (2007), and the Regime Stress Ratio (RSR), which varies continuously from 0 to 3, corresponding to normal (0–1), strike-slip (1–2), and thrust (2–3) faulting stress regimes, is used to visualize the stress regime (Simpson, 1997). The calculation process for both parameters has been embedded into the Tecplot 360 add-on GeoStress (Stromeyer et al., 2020).

4.1.1. Stress state at 2 km depth

A resampling scheme with grid spacing of 15 km × 15 km by averaging the stress orientation within each grid cell (Mardia and Jupp, 2000) is adopted to analyze the orientation of S_H. Fig. 3 shows the averaged orientation of S_H at 2 km depth below sea level. It can be seen that S_H is generally oriented in NW-SE, with a gradual lateral change from NW-SE in the east to NNW-SSE or nearly N-S in the west, consistent with the result of Wen et al. (2001). In the eastern part of the study area, the NW-SE compression is oblique to the ENE-trending faults at high angles, such as the Heyuan fault (F13), Zijin-Boluo fault (F11), and Wuhua-Shenzhen fault (F10), causing this group of faults to experience strong compression perpendicular to the fault strike with a slightly right-lateral strike-slip component of motion (Li et al., 2024b). In the central part of the study area, the NW-SE compression is nearly parallel to the NW-trending faults, such as the Wenchong fault (F20), Baini-Shawan fault (F23), and Xijiang fault (F24), indicating that the NW-trending group of faults experiences strong extension in the NE-SW direction, perpendicular to the fault strike. Toward the west, the S_H orientation becomes nearly N-S and again oblique to the NE-SW faults, such as the Wuchuan-Sihui fault (F32), resulting in left-lateral strike-slip motion on these faults (Li et al., 2024b). The opposite senses of slip on the two fault groups in the east and west of the GBA region, inferred from the orientations of the fault relative to S_H, agree well with field observations (Huang and Zheng, 2001; Fan et al., 2022).

Abrupt disturbances in local stress orientation mainly occur in the middle segment of the Kaiping-Enping fault zone (F26, F28) and the Wuchuan-Sihui fault (F32). The high curvature and close spacing characteristics of these lithospheric scale faults may contribute to the abrupt disturbance in local stress orientation near the faults.

There are also some rotations of S_H near the middle of the western and the eastern boundaries (22°-22.5°N), oriented radially eastward or westward, but they are more gradual (Fig. 3). Boundary effects are unlikely to be the cause of this variation, as at least the western boundary of the model is well constrained by relatively uniformly distributed GPS data (Wang and Shen, 2020). Furthermore, our study area has been shrunk inward by ~50 km to minimize such effects (Fig. 2). The good consistency between our modeled S_H orientations and those from in-situ stress measurements and FMS data (Fig. 3) suggests that the modeled local variations in S_H orientation near the middle of the eastern and the western boundaries are likely genuine.

The background color in Fig. 3 shows the stress regime pattern at a depth of 2 km in the GBA region. The RSR parameter is employed to categorize the tectonic regime. Generally, the study area is dominated by strike-slip and thrust faulting regimes. Roughly delineated by the Wuchuan-Sihui fault (F32), the Guangzhou-Conghua fault (F25), and the Heyuan fault (F13), the southeastern part is characterized by a transpressional or thrust faulting stress regime (RSR > 2), while the

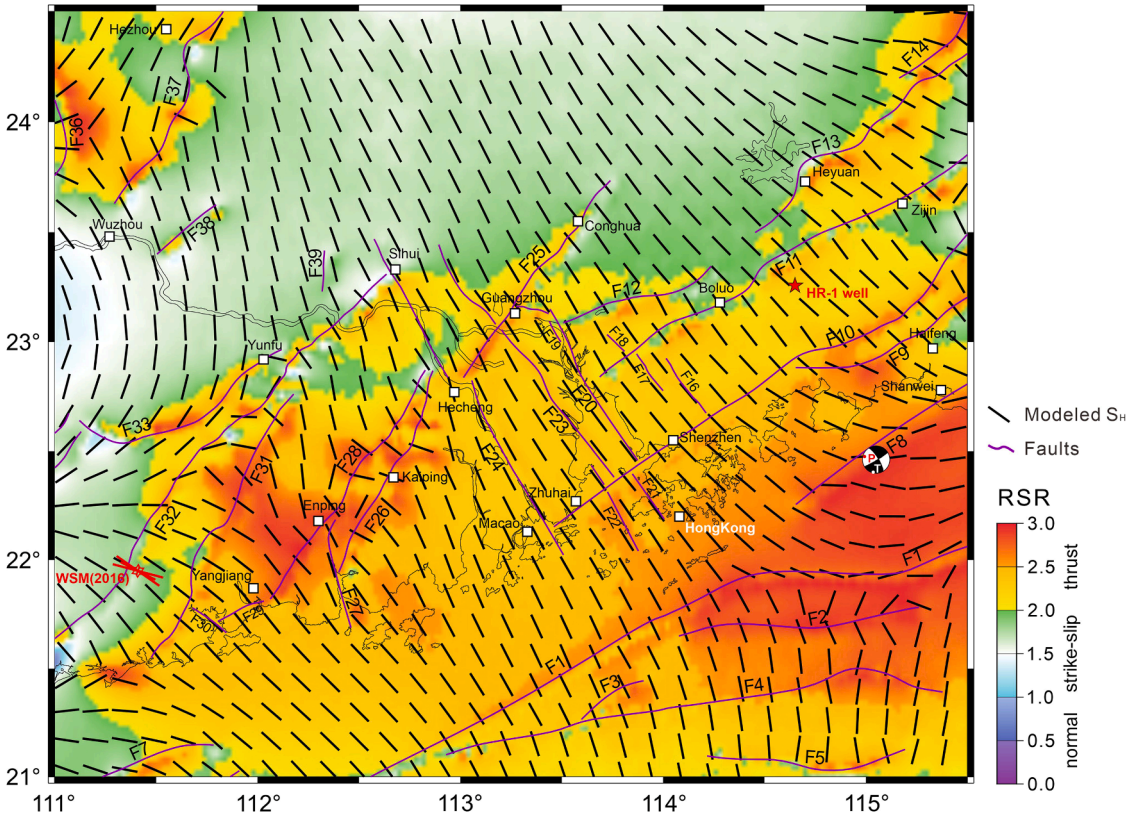

Fig. 3. Modeled S_H orientation and stress regime at 2 km depth below sea level. Black bars represent the modeled S_H orientation. Grid spacing is 15 km × 15 km. Magenta lines show the fault traces implemented in the model. The red star indicates the location of the HR-1 geothermal well. The P axis of the FMS of the M_S4.2 earthquake which occurred on 2022–03–13 and the stress records from the WSM database (red bars) compare well with the modeled S_H orientation. Thin black curves represent coastlines. RSR - Regime Stress Ratio as a measure for tectonic regime (Simpson, 1997).

northwestern part exhibits a strike-slip faulting stress regime with a thrust component (1.5 < RSR < 2.0) (Fig. 3). In the southeastern part, the modeled stress regime agrees with in-situ stress measurements conducted in the HR-1 well and Hong Kong at depths of less than 3 km (Lai et al., 2019; Zhang et al., 2023). In the northwestern part, although few model-independent in-situ stress data are available to validate the model results, the higher elevation in this area (see Fig. 1) implies an enhanced vertical loading, which can transfer the stress regime from thrust faulting to strike-slip faulting. In general, at the depth of 2 km shown here, the crustal stress state can still be influenced by the regional topography (Liu and Zoback, 1992). Therefore, the observed variation in stress regime from thrust faulting in coastal areas to strike-slip faulting inland shown in Fig. 3 is reasonable.

4.1.2. Stress state at 10 km depth

Fig. 4 shows the stress orientation and stress regime pattern at a depth of 10 km in the study area. Generally, the S_H orientation changes from NW-SE in the east to nearly N-S in the west. The S_H orientation and its lateral variation are almost the same as those at 2 km depth, except in some local areas, such as the middle of the Kaiping-Enping fault zone (F26, F28), where the divergence in stress orientation is less pronounced than that at 2 km depth, showing a relatively consistent orientation with the surrounding area. We attribute this reduced divergence to the greater planarity of the fault surface at depth.

However, the stress regime at 10 km depth is very different from that at 2 km. Fig. 4 shows that most of the study area is dominated by a strike-slip faulting stress regime with a tendency towards normal faulting. Obvious variations in stress state occur along faults. The stress in the hanging wall tends to have an additional thrust component, while the stress in the footwall tends towards normal faulting. This is particularly evident on the SE-dipping Zijin-Boluo fault (F11), the NW-dipping Wuhua-Shenzhen fault (F10), and the NW-dipping Enping fault (F28). The width of these variations is typically around 15 km and narrows as the fault dip steepens (Fig. 4). The study area also features other local stress anomalies. Notably, a significant local normal faulting stress field (RSR < 1) is present in the middle segment of the Wuchuan-Sihui fault (F32) and the northern segment of the Zhigong fault (F31). Additionally, a thrust stress regime is situated between the Chaozhou-Shanwei fault (F8) and the Littoral fault (F1). These stress anomalies cover relatively large areas and their centers are located some distance from the faults themselves.

4.2. Stress state on the 3D fault system

The normal stress (S_n) on fault surfaces is calculated from the local stress tensor. Here, we only focus on the stress state at depths shallower than 10 km, which holds the majority of seismic activity and almost all exploitable geothermal resources in the GBA region (Xia et al., 2022; Wei et al., 2024c).

Fig. 5a shows the normal stress distribution on each fault of the 3D fault system. The normal stress increases with depth, but the gradient varies with fault strike. The gradients on the NE- and ENE-trending faults are greater than those on the NW-trending faults, resulting in generally higher normal stresses on the NE and ENE-trending faults at a given depth (Fig. 5b and c). Fig. 5b shows the extracted normal stress on the fault surface at 9 km depth. This depth is chosen over 10 km primarily because it is shallower than the lower termination of the NW-trending faults (which lies between 9 and 10 km), allowing us to analyze stress on all faults in the model.

From Fig. 5b, it can be observed that the normal stress on the ENE-trending faults in the eastern part is the highest, ranging from 260 MPa to 320 MPa. The normal stress at the same depth on the NW-trending faults in the central part is the lowest, at less than 240 MPa. The NE-trending faults in the western part generally exhibit intermediate normal stress values, although some areas show higher stress. This pattern is also evident in 2 km depth normal stress slice (Fig. 5c). We

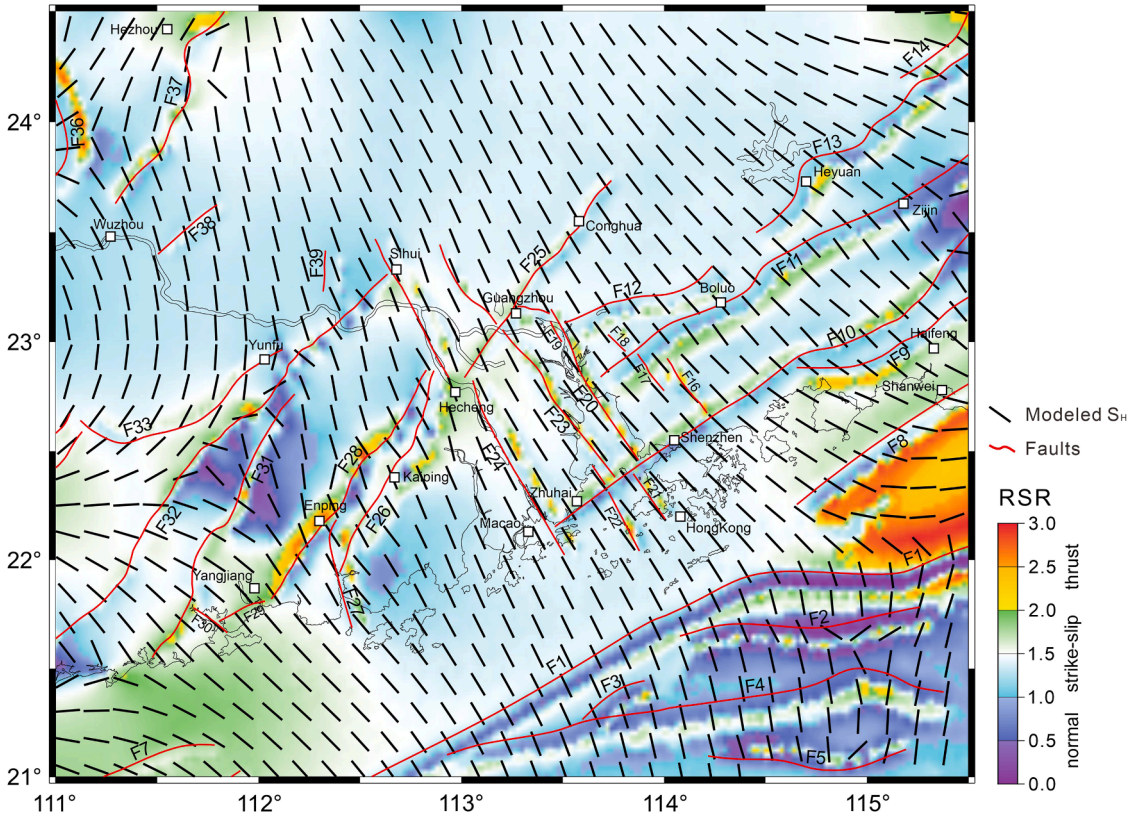

Fig. 4. Modeled S_H orientation and stress regime at 10 km depth below sea level. Black bars represent the modeled S_H orientation. Grid spacing is 15 km × 15 km. Red lines show the fault traces implemented in the model. Thin black curves represent coastlines.

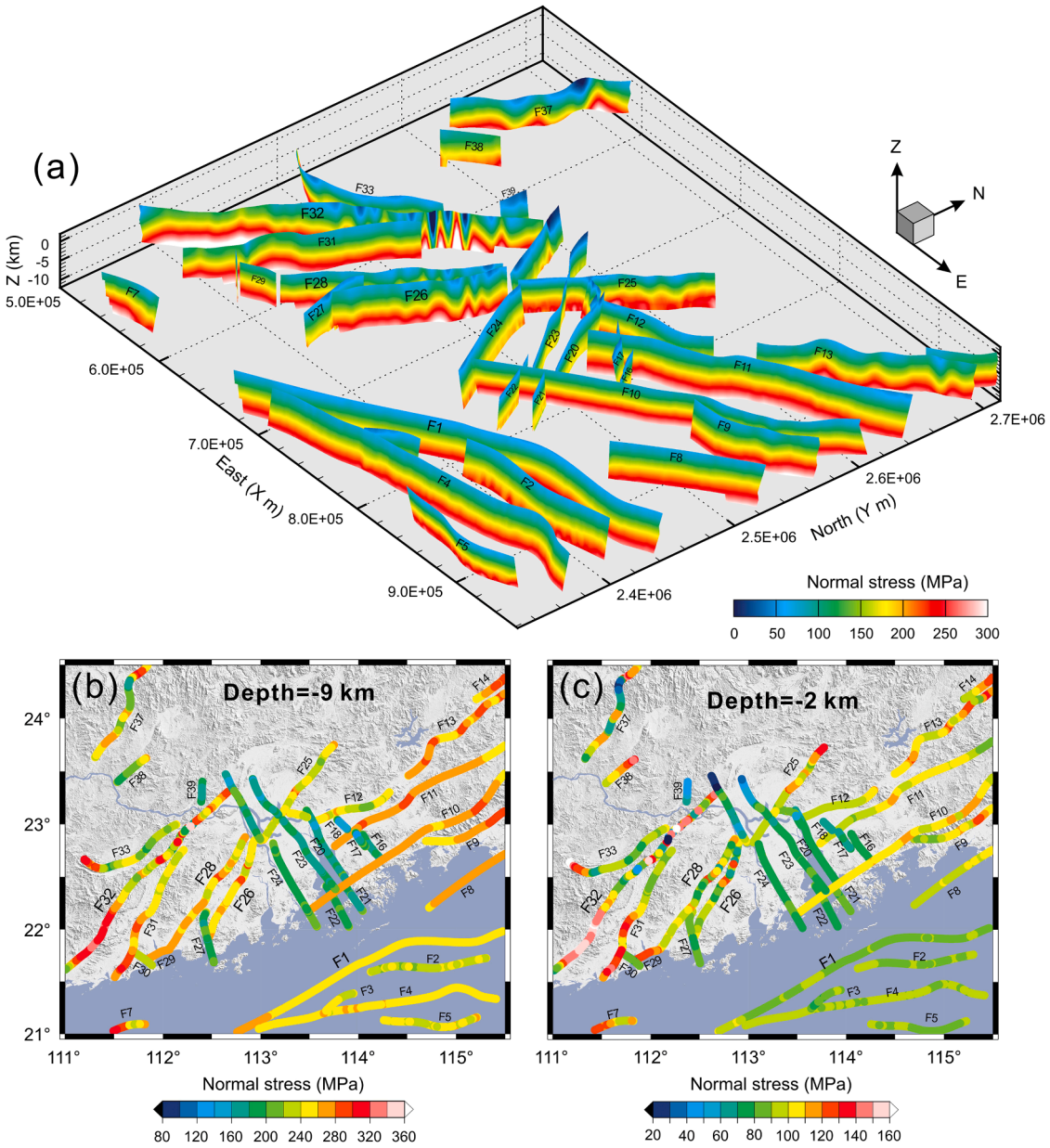

Fig. 5. Distribution of normal stress (a) on the 3D fault surfaces and on faults at depths of (b) 9 km and (c) 2 km below sea level.

attribute this variation in normal stress with fault strike to the regional variation in S_H orientation relative to the fault strike. Because S_H is oriented obliquely or nearly perpendicular to the NE- and ENE-trending faults, these faults experience greater compression than the NW-trending faults, which are nearly parallel to the S_H.

In addition, for individual faults, lateral variations in normal stress are primarily concentrated in local areas where fault geometry changes significantly (e.g., F32, Fig. 5a). Alternating zones of abnormally high and low normal stresses occur along these segments of high local curvature. Conversely, where the fault surface is relatively straight, the normal stress variation along the fault is less pronounced. This is typically seen on the Wuhua-Shenzhen fault (F10) and the Zijin-Boluo fault (F11) (Fig. 5).

4.3. Slip tendency and dilation tendency

Faults with high shear stress and dilation are known to be highly permeable structures that can act as conduits to enhance fluid flow (Barton et al., 1995; Ferrill and Morris, 2003). Therefore, it is common practice to analyze the slip and dilation tendency of faults to identify and assess geothermal systems (e.g., Moeck et al., 2009; Jolie et al., 2015, 2016; Dávalos-Elizondo and Laó-Dávila, 2023). According to Morris et al. (1996) and Ferrill et al. (1999), slip tendency (T_S) and dilation tendency (T_D) are quantified by $T_S=\tau/S_n$ and $T_D=(\sigma_1- S_n)/(\sigma_1- \sigma_3)$, where τ is shear stress, S_n normal stress, σ_1 the maximum principal stress, and σ_3 the minimum principal stress. The value of T_S is equal to the coefficient of static friction for a cohesionless fault and is not normalized by the friction coefficient assumed for the faults. All of these stress values are derived from the modeled stress field. The slip and dilation tendency analysis of faults is performed at a depth of 2 km, which is in the middle of the depth range of fluid circulation in the study area (Yuan et al., 2022; Li et al., 2023; Tian et al., 2023; Wei et al., 2024c). The results are mapped in Fig. 6.

The overall slip tendency on the faults is relatively low (<0.2) (Fig. 6a), except for some high slip tendency anomalies at the fault tips, which are due to the elastic rock properties used in the model. Faults oriented in ENE-WSW generally have the highest slip tendencies (up to 0.2), while NW-trending faults have the lowest. In contrast, the dilation

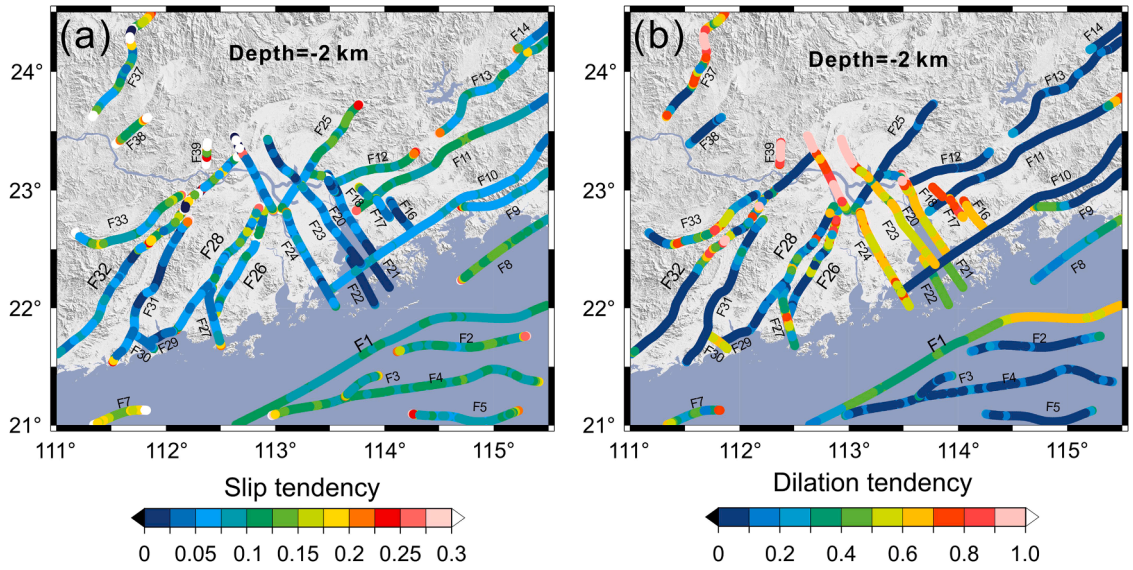

Fig. 6. (a) Slip tendency and (b) dilation tendency on the faults in the GBA region at a depth of 2 km below sea level.

tendency is the highest on NW-trending faults (0.5–1.0) and lowest on ENE-trending faults (Fig. 6b). The FMSs in the area indicate that seismogenic faults responsible for normal faulting earthquakes are usually NW-trending, while those for strike-slip earthquakes are mostly ENE-trending (Fig. 10). These kinematic patterns of the faults revealed by the FMSs support the modeled slip and dilation tendencies. This comparison is based on the assumption that the kinematics of faults at depth are consistent with those at shallower depths, although most of the FMSs are from depths greater than the 2 km analysis depth. In the west, NE-trending faults consistently exhibit alternating high and low slip and dilation tendencies along their strikes (e.g., F32, F26, F28; Fig. 6). We attribute these variations to significant local changes in fault geometry, similar to the alternating changes in normal stress on these faults described in Section 4.2. The average slip tendency and dilation tendency for faults with different orientations are summarized in Table 1.

4.4. Stress analysis of individual faults

According to fault strike, the faults in the GBA can be classified into three groups: ENE-trending, NE-trending, and NW-trending faults. These are primarily located in the eastern, western, and central parts of the study area, respectively (Fig. 1). In this section, we select a representative fault from each group to illustrate the detailed stress state features on the fault surface, including the S_H orientation near the fault, as well as the distribution of normal stress and slip-dilation tendency (T_S+T_D) on the fault surface.

Table 1
Average slip tendency and dilation tendency on faults at a depth of 2 km.

Fault orientation	Fault number	Average slip tendency (T_S)	Average dilation tendency (T_D)
NW-trending	F16	0.03	0.68
	F17	0.06	0.71
	F18	0.08	0.74
	F19	0.03	0.77
	F20	0.03	0.68
	F21	0.02	0.44
	F22	0.02	0.51
	F23	0.04	0.70
	F24	0.10	0.71
ENE-trending	F8	0.12	0.28
	F9	0.08	0.16
	F10	0.07	0.03
	F11	0.10	0.10
	F12	0.11	0.07
	F13	0.09	0.07
	F14	0.07	0.06
NE-trending	F25	0.09	0.07
	F26	0.10	0.33
	F28	0.09	0.21
	F31	0.05	0.06
	F32	0.14	0.19

4.4.1. The ENE-trending Heyuan fault

The Heyuan fault (F13) is part of the southwestern segment of the Heyuan-Shaowu fault zone (Fig. 1), which extends approximately 600 km (Xu et al., 2016). Seismic tomography suggests that the fault dips southeastward with steeper dips near the surface and gentler dips at depth (Ye et al., 2016), indicating it is a listric fault. In our model, we simplified the fault geometry to a constant dip angle of 70° (Li et al., 2024b), preserving the first-order feature of the fault's geometry. Strong hydrothermal activities are present along the Heyuan fault, with many surface manifestations, including large silicified quartz reefs (Fig. 7a) (Tannock et al., 2020a) and numerous hot springs distributed along the fault (Tannock et al., 2020b). Earthquake activity is concentrated primarily in the southwestern segment of the fault, near Heyuan City (Fig. 1). Among these earthquakes, the largest is the 1962 Xinfengjiang *M*6.1 earthquake, which is believed to have been triggered by the Xinfengjiang Water Reservoir (Ding et al., 1983; Gupta, 2002).

Fig. 7a shows the orientation of S_H near the fault. Overall, S_H intersects the Heyuan fault at a high angle, but this angle decreases laterally, from nearly perpendicular in the SW segment to about 60° in the NE segment. This variation in the orientation of S_H relative to the fault will cause a decrease in normal stress (Fig. 5b, Fig. 5c and Fig. 7b) and an increase in shear stress from SW to NE. The acute angle between the fault and the S_H orientation indicates a right-lateral shear sense on the fault, which has been described in the complementary paper focusing on model kinematics (Li et al., 2024b). Some large quartz reefs, which reflect paleo-hydrothermal activities, are exposed at releasing fault bends (Fig. 7a).

Fig. 7b shows the distribution of normal stress on the fault surface. It is evident that the normal stress increases with depth. At 3 km depth, the simulated normal stress values range from 110 to 130 MPa, which is comparable to the S_H values of 110–115 MPa measured in granite core samples from the bottom of the HR-1 well (~3 km below ground surface) using an anelastic strain recovery method (Zhang et al., 2023). This well is located in the south the Heyuan fault, within a short distance of 30 km from the fault trace (see Fig. 1). In our model, the difference in S_H

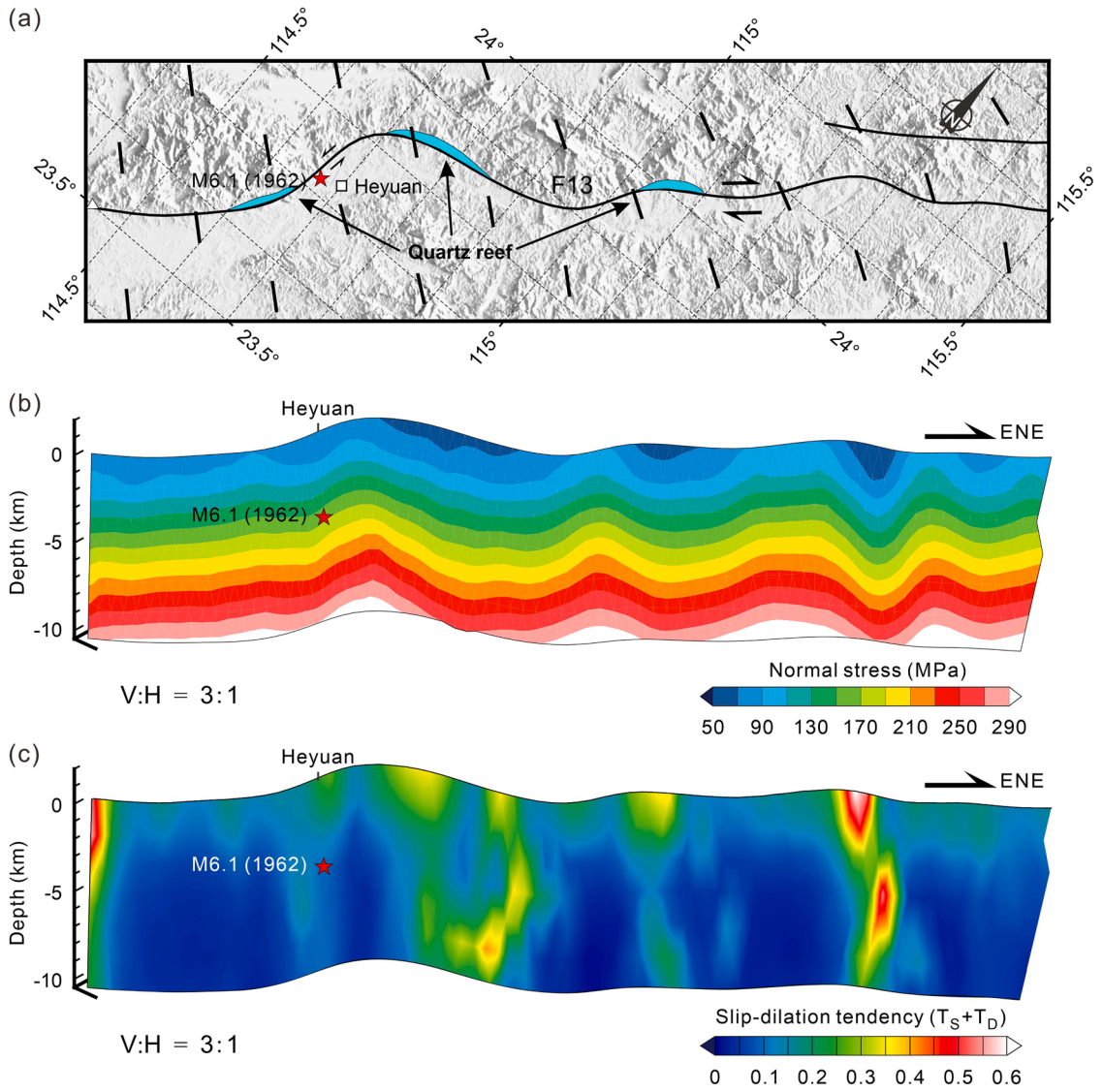

Fig. 7. Modeled stress state on the Heyuan fault (F13). (a) Map view of S_H orientations (black bars) in the vicinity of the Heyuan fault. Ice blue areas along the releasing bends represent the locations of silicified quartz reefs (Tannock et al., 2020a). (b) Distribution of the normal stress on the Heyuan fault. (c) Distribution of the slip-dilation tendency (T_S+T_D) on the Heyuan fault. The vertical to horizontal scale ratio in (b) and (c) is 3:1. Red stars in (a-c) mark the hypocenter location of the 1962 Xinfengjiang *M*6.1 earthquake.

magnitudes and normal stress magnitudes on the fault surface is very small due to the high-angle intersection of S_H with the fault strike (Fig. 7a).

Another notable feature is the significant lateral variation in normal stress along the fault strike (Fig. 7b). These variations are concentrated at local fault bends. Given the right-lateral strike-slip sense of the fault (Li et al., 2024b), these high and low normal stress zones generally correspond to restraining and releasing bends, respectively (Fig. 7b). The locations of low normal stress align with the presence of thick quartz reefs, indicating that the modeled crustal stress can effectively identify the pathways of geothermal fluids. The 1962 Heyuan *M*6.1 earthquake occurred at a restraining fault bend where the modeled normal stress is increased (Fig. 7b), possibly forming an asperity.

Fig. 7c shows the distribution of the sum of slip and dilation tendencies (T_S+T_D) on the fault surface. Overall, the slip-dilation tendency is low (T_S+T_D < 0.3). Relatively high values are mainly located at the releasing bends, consistent with the distribution of low normal stress (Fig. 7b). At these releasing bends, slip-dilation tendencies are generally greater than 0.3, with the highest value of 0.6 located at the bend in the ENE. Additionally, the model results show that high slip-dilation tendencies at the bends can extend to depths of about 10 km, suggesting that these bends can act as conduits for transporting hydrothermal fluids from deeper to shallower levels.

4.4.2. *The NE-trending Wuchuan-Sihui fault*

The Wuchuan-Sihui fault (F32) originates at Haikang Port in Leizhou City, extends northeastward through Wuchuan and Sihui, and connects with the Dayu-Nancheng fault and the Ganjiang fault north of Shaoguan City, spanning approximately 670 km in total (Fig. 1) (GBGM, 1988, p. 760). In our model, only the southwestern segment between Wuchuan and Sihui (approximately 250 km) is implemented, mainly because this segment is more prominent and continuous at the surface (Xu et al., 2016). A deep seismic sounding profile crossing this fault reveals that it extends to the Moho (Zhang et al., 2018). Therefore, we modeled it as a lithospheric scale fault that penetrates the entire depth of the model (Li et al., 2024b). Hot springs are mainly located in the southwestern segment of the fault, with generally low temperatures (<81 °C) (Wei, 2001, p. 72).

Fig. 8a shows significant variations in the orientation of S_H along the fault. The S_H is nearly perpendicular to the fault strike near the ends of

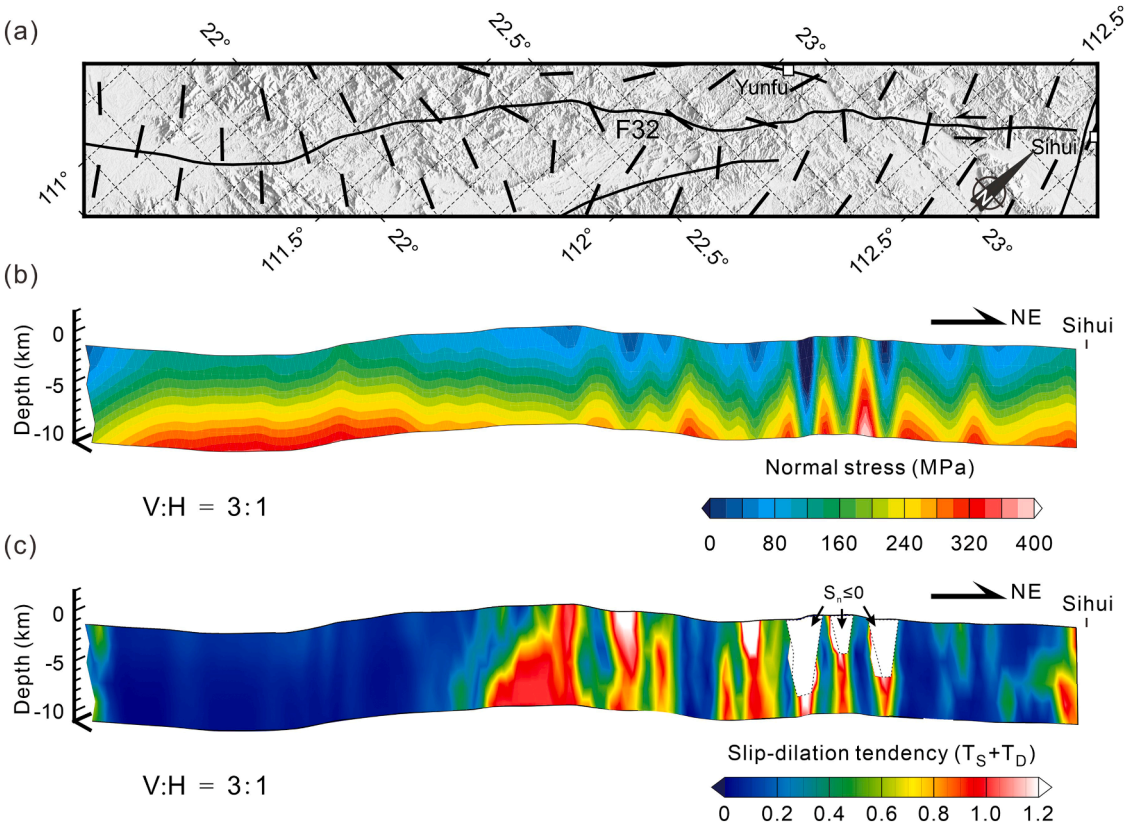

Fig. 8. Modeled stress state on the Wuchuan-Sihui fault (F32). (a) Map view of S_H orientations (black bars) in the vicinity of the Wuchuan-Sihui fault. (b) Distribution of the normal stress on the Wuchuan-Sihui fault. (c) Distribution of the slip-dilation tendency (T_S+T_D) on the Wuchuan-Sihui fault. Three arrows show the locations of fault bends with negative normal stresses, which indicate that the bends are dominated by extension. The vertical to horizontal scale ratio in (b) and (c) is 3:1.

the fault, whereas it intersects the fault at a small angle in the middle segment. This distribution suggests higher normal stress near the ends and lower normal stress in the middle, as shown in Fig. 8b. Pronounced alternations between high and low normal stress are particularly evident in the northeastern segment (Fig. 8b), which is inferred to result from the significant curvatures of shallow fault bends. Low normal stresses imply high dilation tendencies, while high normal stresses indicate low dilation tendencies, as clearly shown in Fig. 8c. The slip-dilation tendency in the middle section of the fault reaches up to 1.0 and can exceed 1.2 at local fault bends, with the dilation tendency being the dominant (see Fig. 6). Three areas with distinct high slip-dilation tendencies located at local fault bends (outlined by dashed polygons) are dominated by negative normal stresses, which indicate that these local fault bends are under significant extension.

4.4.3. The NW-trending Baini-Shawan fault

The NW-trending Baini-Shawan fault (F23) (Fig. 9) is located in the Pearl River Estuary region in the central part of the study area (Fig. 1). This fault spans 150 km in total, starting northwest from Baini, crossing southeastward through the Guangzhou-Conghua Fault (F25) and finally entering the Pearl River Estuary sea area (Xu et al., 2016). The northern segment of the Baini-Shawan fault controls the eastern boundary of the Sanshui basin, where sediment thickness is in the range of 6–7 km based on crustal shear-wave velocity (Lv et al., 2022). In our model, the Baini-Shawan fault is classified as an upper crustal fault, extending down to the base of the upper crust (9–10 km). The existence of many calcite veins in the middle segment of the fault, ranging from 0.2 to 0.8 m in width and formed in the late Pleistocene, indicates significant extension on this fault (Dong et al., 2016). Two normal faulting earthquakes with magnitudes of 3.7 and 4.4 occurred near the northwest segment of the fault in 1997, with nodal planes oriented NW-SE, parallel to the strike of the Baini-Shawan fault (Fig. 10). This indicates that extension remains active, although it was speculated that these earthquakes were induced by water injection and pumping processes during salt mining (Wei, 2001, pp. 363–371).

Fig. 9a shows the NW-SE oriented S_H parallel or at an acute angle to the Baini-Shawan fault strike. This relationship between the orientation of S_H and the fault strike facilitates fault opening. The modeled maximum normal stress on the Baini-Shawan Fault is approximately 220 MPa (Fig. 9b), which is considerably lower than the maximum normal stress values on faults with other orientations (Fig. 7b, Fig. 8b). Overall, the variation of normal stress along the fault strike is gradual, especially in the southeastern segment, where the normal stress contours are nearly horizontal (Fig. 9b). Compared to the southeastern segment, the northwestern segment exhibits a gradual decrease in normal stress, with the minimum value located at the northwestern end of the fault (Fig. 9b). The lower normal stress on the northwestern segment corresponds to higher slip-dilation tendencies, as shown in Fig. 9c. The slip-dilation tendencies on the northwestern segment are as high as 1.0–1.2 and dominate most of this segment. The tendency values on the southeastern segment are somewhat reduced but still generally above 0.6. The slip-dilation tendency on the Baini-Shawan fault is significantly higher than that on faults with other orientations (Fig. 7c, Fig. 8c). The high slip-dilation tendency may account for the normal faulting earthquakes in the northwestern segment (Fig. 10) and the extensional fractures that are filled with calcite in the fault (Dong et al., 2016).

5. Discussion

5.1. Model results verification

The 3D geomechanical model established in this study provides both

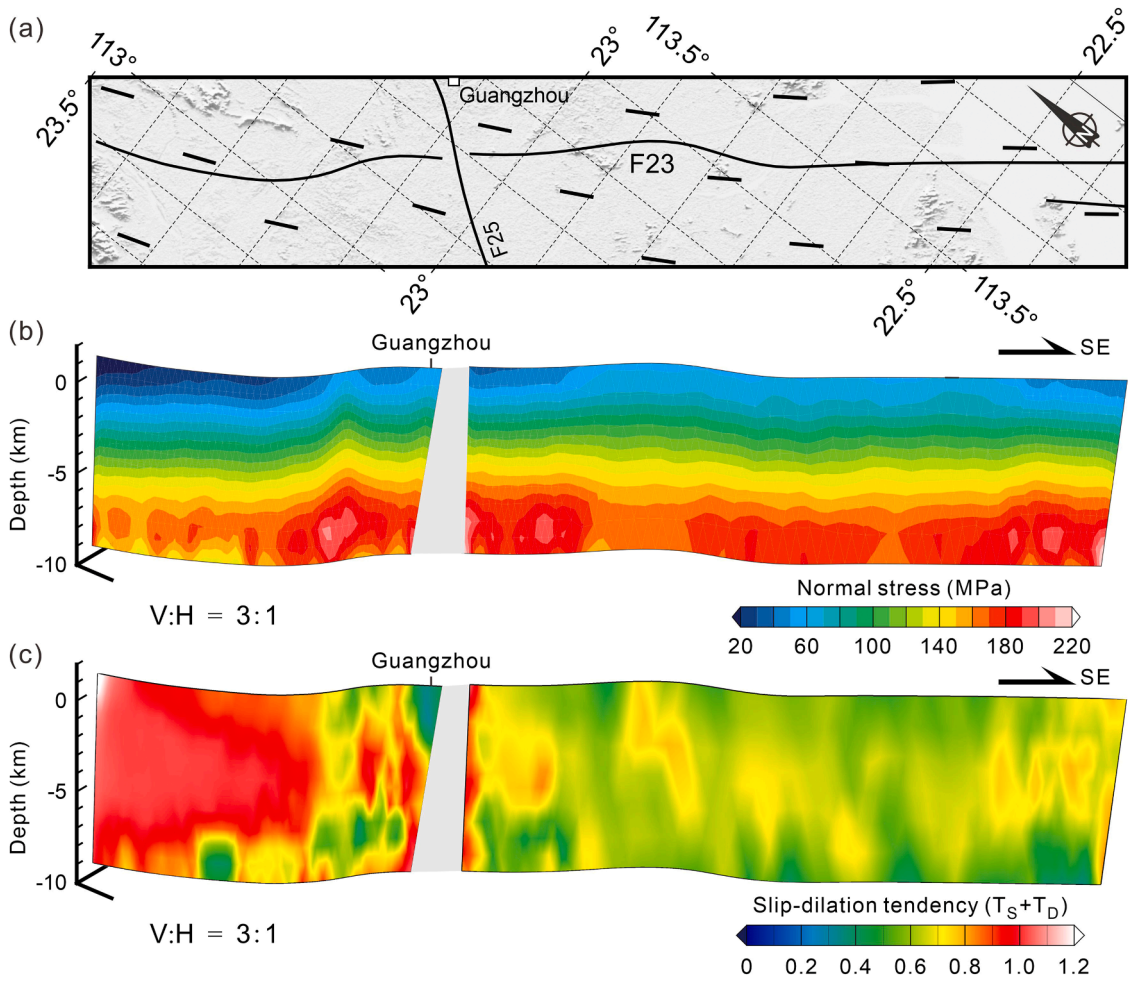

Fig. 9. Modeled stress state on the Baini-Shawan fault (F23). (a) Map view of S_H orientations (black bars) in the vicinity of the Baini-Shawan fault. (b) Distribution of the normal stress on the Baini-Shawan fault. (c) Distribution of the slip-dilation tendency (T_S+T_D) on the Baini-Shawan fault. The vertical to horizontal scale ratio in (b) and (c) is 3:1.

kinematic and dynamic results that can be aligned with observational data. In this section, we compare the modeled stress results with model-independent S_H orientations and FMSs to evaluate the model.

5.1.1. Comparison with model-independent S_H orientations

The World Stress Map project (WSM) compiles global S_H orientation data and categorizes these data into different qualities (A–E) based on their standard deviations (Heidbach et al., 2018). According to the WSM quality ranking scheme (Heidbach et al., 2010), the A-quality has the highest accuracy with a standard deviation of ±15°, and the accuracy of B-, C- and D-quality decreases successively with ±20°, ±25° and ±40° standard deviation, respectively. The lowest quality is E-quality, which has standard deviations greater than ±40°. It is suggested that A-, B-, and C-quality data are commonly reliable for use in stress analysis (Heidbach et al., 2010). Therefore, we only select the stress data of quality A-C to validate the model.

There are only nine WSM stress data in the study area, comprising three B-quality and six C-quality records (Fig. 10). These records are sparsely distributed across five locations and are primarily obtained from FMSs and in-situ stress measurements (overcoring, hydraulic fracturing) (Fig. 10). There are no WSM stress data records available for the center of the study area. To enhance data coverage, we further gathered stress orientation data from published literature, totaling 13 records, which include 12 P-axes orientations (Kang et al., 2008) and one in-situ stress measurement conducted in a 3 km deep borehole (Zhang et al., 2023). This expanded dataset provides improved spatial coverage for comparison (Fig. 10), although some local data gaps remain due to the lack of additional available data.

The model-independent S_H (including P-axis) orientations from the WSM database and published literature generally trend NW-SE (Fig. 10), which are consistent with the modeled S_H orientations. The deviation angles between them, as shown in Fig. 11a, range from 0° to 60°, with a mean deviation of 25°. The stress data used for comparison are either quality B and C (WSM) or primarily estimated from P axes of FMSs (Kang et al., 2008), which generally have a deviation range of ±25° based on the WSM quality ranking scheme (Heidbach et al., 2010). Accordingly, the mean deviation angle (25°) is still within the standard deviation range of the model-independent S_H orientations. Therefore, the modeled S_H orientations can be considered comparable to the model-independent records.

5.1.2. Comparison with FMSs

FMS is another important data source that can be used not only to reveal the geometry and kinematic characteristics of the ruptured fault, but also to obtain valuable insights into the stress regime at deeper depths. We collect records of 55 existing FMSs within the study area and calculate 15 new FMSs using the gCAP method (Zhu and Ben-Zion, 2013) to improve data coverage (Table S1). Figure S1 illustrates an example of the good consistency between the FMS calculated in this study and the one published previously. The distribution of these FMSs is shown in Fig. 10.

These FMSs can be classified into four faulting types according to the

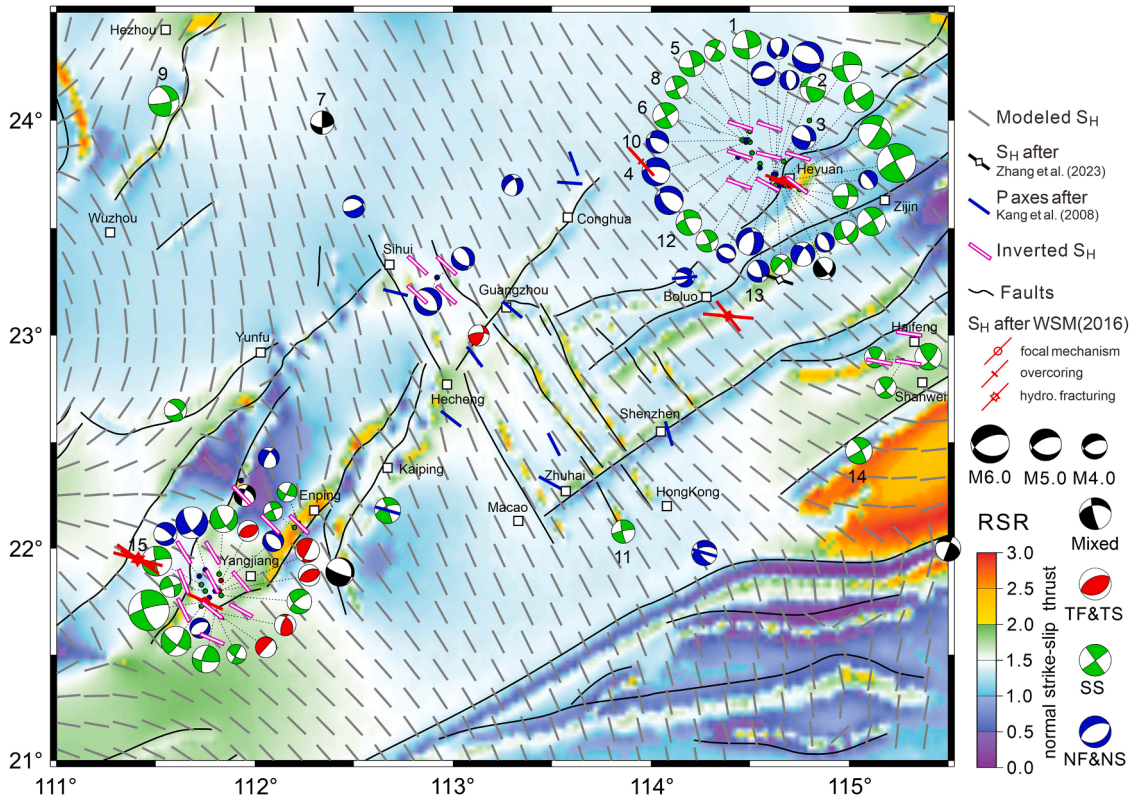

Fig. 10. Comparison of the modeled S_H orientation and stress regime at 10 km depth with model-independent stress data. The model-independent data include stress records from the WSM (red bars with symbols) (Heidbach et al., 2018), in-situ stress measurements (the black bar with a white diamond in the middle) (Zhang et al., 2023), P axes (blue bars) (Kang et al., 2008), focal mechanism solutions (Kang et al., 2005a; the numerated ones are calculated by this study), and inverted S_H based on the focal mechanism solutions (hollow magenta bars) (this study). TF&TS, thrust or thrust oblique faulting; SS, strike-slip faulting; NF&NS, normal or normal oblique faulting.

stress regime classification criteria (Zoback, 1992). They are strike-slip faulting (34 out of 70), normal faulting (25), thrust faulting (6) and mixed faulting (5). It is evident that the distribution of these FMSs supports the view that the GBA region is dominated by a transtensional stress regime, which is comparable to the modeled stress regime (Fig. 10). The good consistency is particularly evident in two places. One is in the northeastern part of the study area, particularly in the Heyuan area, where FMSs predominantly indicate strike-slip and normal faulting (Fig. 10), consistent with the modeled stress regime dominated by strike-slip faulting with a tendency towards normal faulting ($1.0 < RSR < 1.5$). The other is in the southwestern part of the study area, particularly in the Yangjiang area, where earthquakes are mainly strike-slip and thrust faulting events (Fig. 10), consistent with the modeled strike-slip stress regime with a tendency towards thrust faulting ($1.5 < RSR < 2.0$).

We further inverted the S_H orientation from these FMSs using the MSATSI program (Hardebeck and Michael, 2006; Martínez-Garzón et al., 2014), which can invert FMS data to determine the stress field using a damped linear stress inversion method. The grid used for S_H inversion is identical to that used for the modeled S_H (15 km × 15 km grid spacing), facilitating direct comparison. The more FMS data are within each grid cell, the better the estimation of the stress axes is. However, the spatial distribution of the FMS data remains sparse relative to the large study area. To balance the scarcity of data with the accuracy in stress inversion, we only inverted stress results for grid cells containing two or more FMSs for further comparison. These inverted S_H orientations generally trend in the NW-SE direction, as depicted by the hollow magenta bars in Fig. 10. We also calculate the orientation deviation angles between the modeled and the inverted S_H, following the procedure outlined in Section 5.1.1, and find they range from 0° to 36° with a mean value of 20.8° (Fig. 11b). This mean deviation is smaller than the standard deviation (±25°) of S_H orientations obtained by formal stress inversions of FMSs (Heidbach et al., 2010). Increasing the friction coefficient from 0.02 to 0.6 does not alter the S_H orientation or the foundamental stress regime type, but it tends to smooth out local variations in the stress regime near the fault (Figure S2).

5.2. *Influence of lateral boundary conditions on the modeled stress state*

As mentioned in Section 3 and detailed in the kinematic paper by Li et al. (2024b), the lateral boundary conditions of the model are constrained by velocities derived from GPS records and the model time. The model boundaries on the continental side, including the western boundary, the northern boundary, and the northern segment of the eastern boundary, are well constrained by dense GPS observations (Wang and Shen, 2020). However, the southern boundary and the southern segment of the eastern boundary, located in the South China Sea, are poorly constrained due to the lack of oceanic GPS stations. A single GPS measurement from the Dongsha Islands, near the southeastern corner of the model, indicates that the Dongsha Islands are moving southeastward at a rate of 10.7 mm/a relative to the stable Eurasia Plate (Yu et al., 1999). This velocity, however, is too large to produce a NW-SE oriented S_H that fits the stress observations (Li et al., 2024b). Instead, a relatively low displacement rate should be assigned to the southeastern corner. We therefore choose a value of 6.9 mm/a as the velocity constraint for the southeastern corner (V_{SE}) of the model, while maintaining the ESE direction in line with the original GPS data (Yu et al., 1999). This reduced velocity, inferred from the trend in continental GPS measurements, generates a more appropriate S_H orientation that compares well with the independent stress observations (Fig. 10).

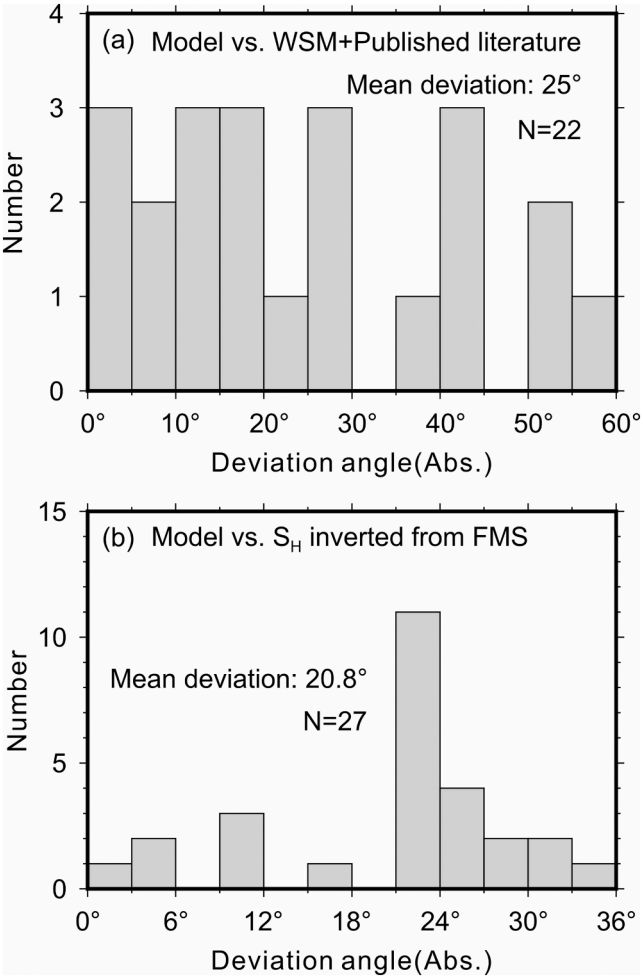

Fig. 11. Histogram of the absolute deviation angle between modeled S_H orientations and the model-independent data actually measured. (a) Model vs. WSM and published literature. (b) Model vs. S_H inverted from focal mechanism solutions (FMSs). N-total number of data.

The impact of adjusting this inferred velocity on the modeled kinematic results has been explored by two additional tests with ± 10 % perturbation to the V_{SE}=6.9 mm/a (Li et al., 2024b). In the following paragraphs, we will further explore the variations in stress based on these two test models.

Fig. 12a shows the S_H orientation and stress regime obtained in Test 1, in which the velocity of the southeast corner of the model is reduced by 10%, i.e., V'_{SE}=0.9V_{SE}=6.21 mm/a. Comparison of the S_H orientation in Test 1 and the originally modeled S_H orientation indicates that in most parts of the study area, the S_H orientations remain unchanged, except for some local areas such as the middle segment of the Wuchuan-Sihui fault (F32) and areas in the South China Sea, particularly in the southeastern corner, where the boundary conditions (V'_{SE}) exhibit the greatest variation (Fig. 12a). Specifically, at Location 1 in the South China Sea (Fig. 12a), the S_H orientation shows a slight counterclockwise rotation (~15°) with respect to the original S_H. This trend becomes pronounced (~46°) in the region south of the Littoral fault (F1) (Location 2). However, at Location 3, the orientation of S_H in Test 1 shows a clockwise rotation relative to the originally modeled S_H (Fig. 12a).

Fig. 12b shows the S_H orientation and stress regime obtained in Test 2, in which the velocity of the southeast corner of the model is increased by 10%, i.e., V'_{SE}=1.1V_{SE}=7.59 mm/a. The S_H orientations on land remain almost unchanged, except for those on the Wuchuan-Sihui fault (F32) and the Kaiping-Enping fault zone (F26, F28). In the South China Sea region, significant changes in stress orientation are also evident, but the sense of rotation through the acute angle from the originally modeled S_H to the S_H in Test 2 is always opposite to that in Test 1 (Fig. 12a).

There are significant differences in stress regimes between these two tests. In Test 1, the stress regime is primarily strike-slip with thrust components (Fig. 12a), which is caused by increased NW-SE compression due to the reduced velocity at the southeastern corner of the model (Li et al., 2024b). In Test 2, the increased V_{SE} drags the southeastern edge of the model faster southeastward, producing extension and causing the stress regime to evolve towards a normal faulting type (Fig. 12b). Since the original stress regime is characterized by a strike-slip faulting type, even small amounts of pushing or pulling at the boundary can easily cause a switch in the principal stress axes, leading to significantly different stress regimes.

In summary, velocity perturbations at the southeastern corner have little effect on the modeled S_H orientation in most onshore areas. The more pronounced changes in S_H orientations are mainly confined to the South China Sea region (where the distance from the perturbation source is relatively small) as well as some local onshore areas. In addition, the reference model and the two test models show consistent stress distribution patterns. These tests indicate that the modeled stress state in this study can be considered reasonable.

5.3. *Implications for geothermal resource exploration*

Stress state has a significant impact on the permeability of rocks, fractures and faults, which in turn affects fluid flow in rock mass (e.g., Kranzz et al., 1979; Morrow et al., 1994; Siler et al., 2018). Therefore, analyzing the stress state on faults can effectively identify structural locations favorable for the formation of geothermal systems (Jolie et al., 2016), especially in the exploration for blind geothermal systems lacking surface manifestations (e.g., Siler et al., 2019).

5.3.1. *Insights from normal stress and slip-dilation tendency on faults*

Under a given crustal stress state, lower normal stress on a fault leads to a higher dilation tendency, promoting a higher fault conductivity and facilitating fluid flow (e.g., Barton et al., 1995). Consequently, faults within extensional or transtensional stress regimes generally have higher permeability, providing favorable channels for the flow and storage of thermal fluids (Moeck, 2014).

In the GBA region, since S_H is generally oriented NW-SE, the normal stresses on the NW-trending faults are lowest (Fig. 5), resulting in significantly higher dilation tendencies on these faults compared to those with other orientations (Figs. 6, 9). Therefore, from a geomechanical point of view the NW-trending faults are more likely to serve as high-permeability conduits for geothermal fluid circulation. The clustered distribution of hot springs along the NW-trending faults provides evidence for this inference (e.g., Luo et al., 2022).

Although the normal stresses on NE- and ENE-trending faults are generally high, significantly lower normal stresses occur locally at fault bends (Figs. 7b, 8b). These lower normal stresses are inferred to result from the strike-slip component of fault movement (Li et al., 2024b), creating local extension at the bends, where fluid pathways can form (e.g., Jolie et al., 2016). For example, the local low normal stresses on the Heyuan fault (F13) with relatively high slip-dilation tendencies are mostly located at the releasing bends, corresponding well with the locations of quartz reefs (Fig. 7), which represent paleo-hydrothermal systems. This strong spatial correlation indicates that the stress state on the Heyuan fault is long-term stable and keeps the fault bends extensional, providing space for precipitation of minerals. These paleo-hydrothermal systems may still be active at present, as manifested by several hot springs originating from the quartz reefs revealed by drilling data (Fang, 2012).

Local fault bends with lower normal stresses and higher slip-dilation tendencies also appear in the middle and northern segments of the Wuchuan-Sihui fault (F32) (Fig. 8). These releasing bends along the NE-

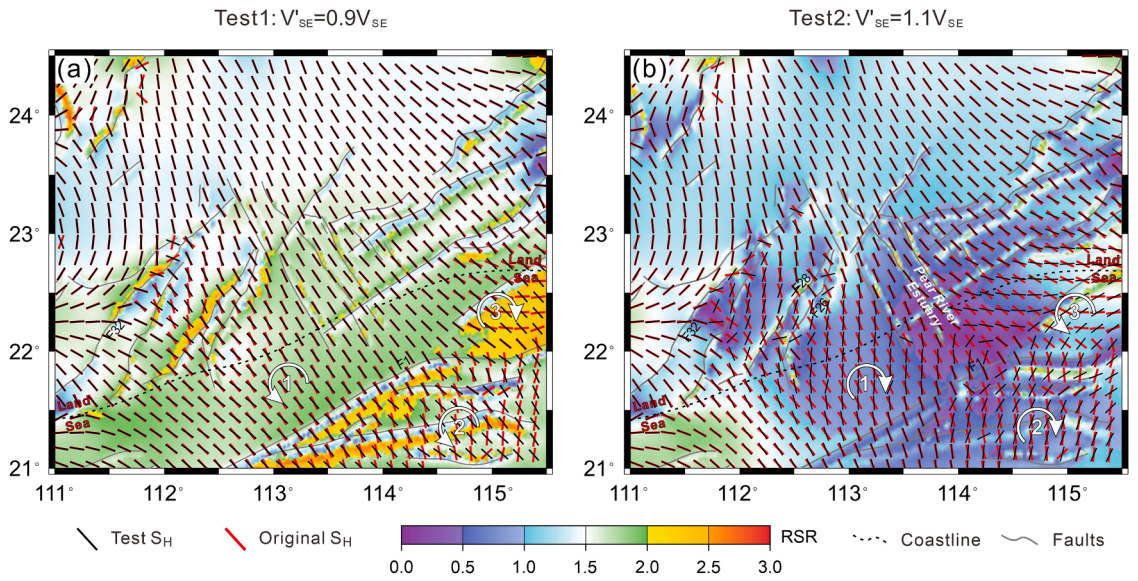

Fig. 12. Comparison between the originally modeled S_H orientation at 10 km depth and that modeled in two tests with variable boundary conditions. (a) Test 1 with -10% perturbation to the velocity at the southeastern corner (V_{SE}) of the original model. (b) Test 2 with +10% perturbation to V_{SE}. Black and red bars represent the test result and the original S_H, respectively. Dashed lines show the coastlines and grey lines are the fault traces. White numbers 1, 2 and 3 indicate locations referred to in the text.

and ENE-trending faults can act as fluid conduits for geothermal circulation, therefore the right-stepping bends (or step-overs) along the ENE-trending faults and the left-stepping ones along the NE-trending faults may be potential sites for geothermal exploration due to the opposite slip senses on these two fault groups (Li et al., 2024b). The Huangshadong geothermal field, formed within a releasing step-over developed along an ENE-trending fault (Fan et al., 2022), exemplifies this proposed geothermal genesis model.

5.3.2. *Insights from depth-dependent stress regime*

Stress regime can also influence fault permeability. Generally, normal faulting stress regime is more likely to create higher permeability (Duwiquet et al., 2022; Chen et al., 2024). In the study area, the crustal stress regime varies with depth. In the shallow crust (e.g., 2 km depth), the stress regime is characterized by transpression (Fig. 3), while at greater depths (e.g., 10 km depth), it changes to a strike-slip faulting regime with a tendency towards normal faulting (Fig. 4). This depth-dependent stress regime results in variable fault permeability with depth. For example, for the large ENE- and NE-trending faults that intersect the NW-SE oriented S_H at high angles, the transpressional stress regime in the shallow crust will make these faults tighter with reduced fault permeability. While at greater depths, the transtensional stress regime would increase the permeability of faults at that depth and facilitate the conducting of heat energy or hot fluids. Consequently, at depth, the NE- and ENE-trending faults can act as conduits for transporting heat energy or hot fluids towards the shallow crust, where their upward movement is impeded by the reduced fault permeability. This impedance can lead to the accumulation of heat and hot fluids beneath the shallow crust, forming geothermal reservoirs along the regional NE- and ENE-trending faults within a certain width. This inference is consistent with the NE-/ENE- trending belts of strong geothermal anomalies observed in the GBA by Xu et al. (2023).

5.3.3. *Conceptual model of geothermal system in the GBA region*

Fig. 13 schematically illustrates the formation mechanism of the geothermal system in the GBA region. The heat source is believed to be the widespread granitoids in the upper crust with notably high radiogenic heat production (Zhou et al., 2020; Lin et al., 2022) and the uplifted mantle corresponding to a shallow asthenosphere (Guo et al., 2019; Dong et al., 2020; Chen et al., 2022). Geochemical investigations of geothermal fluids in the GBA region also indicate that mantle-derived fluids have migrated into the geothermal system (Mao et al., 2018; Luo et al., 2022). The NE- and ENE-trending faults, which are suggested to be of lithospheric scale (Zhang et al., 2018; Dong et al., 2020), have experienced alternating episodes of shortening and extension in the late Mesozoic and control the distribution of granitic rocks (Li et al., 2020). These faults provide conduits for the ascend of heat energy or hot fluids from depth. As these fluids approach the surface, the crustal stress regime changes from transtension to transpression, tending to close the NE- and ENE-trending faults at shallow depths due to their high angle to the S_H orientation, but promoting the opening of NW-trending faults (see

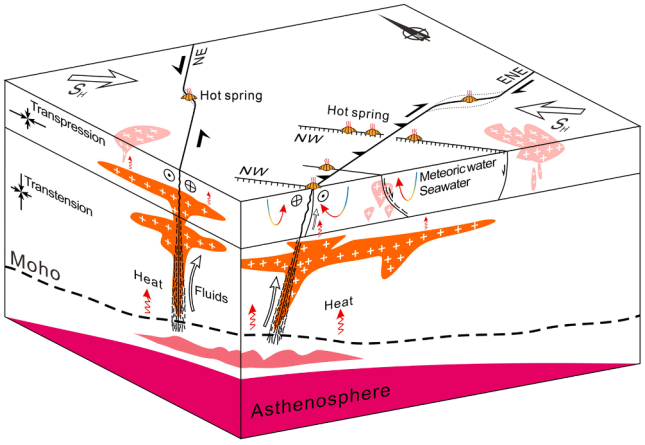

Fig. 13. Schematic diagram of the fault-controlled geothermal systems in the GBA region. View is from SW to NE. The uplifted mantle and the widespread granitoids in the crust jointly provide the heat for the geothermal resources. Hot fluids ascend along the ENE-/NE-trending faults in the deep part of the crust, then shift to upflow along the NW-trending faults in the shallow part, which is due to the variation in fault permeability caused by the transpressional stress regime with an NW-SE S_H in the shallow crust. The intersections of the ENE-/NE-trending faults with the NW-trending faults as well as the releasing fault bends on the ENE-/NE-trending faults, are considered favorable locations for prospective geothermal systems.

Fig. 9). The hot fluids then change to upflow along the secondary NW-tending faults, mixing with meteoric water and seawater (Wei et al., 2024a), and eventually forming clusters of hot springs (e.g., Luo et al., 2022). Releasing bends or step-overs along the NE- and ENE-trending faults with relatively high strike-slip components can also provide favorable pathways for geothermal upwelling, as exemplified by the Huangshadong geothermal field (Fan et al., 2022).

5.4. Implications for seismic hazard assessment

Fluid injection or production during subsurface operations, whether in a hydrothermal system or an Enhanced Geothermal System (EGS), will alter pore pressures and can trigger earthquakes on critically-stressed faults (Evans et al., 2012). Although most of the induced earthquakes are small or unfelt, they can also be damaging events with magnitudes up to M_W 5.4 (e.g., Kim et al., 2018) if the accumulated strain energy is high enough, for example, within a high background crustal stress environment (Lu et al., 2024). The occurrence of three strong earthquakes with magnitudes greater than 6.0 in the GBA region—namely, the 1911 Honghai Bay *M*6.0 earthquake, the 1962 Xinfengjiang *M*6.1 earthquake, and the 1969 Yangjiang *M*6.4 earthquake—indicates that the faults in the area may be critically stressed (Yao and Chen, 1990). Therefore, it is necessary to conduct seismic hazard assessment before and during geothermal energy production, especially in economically developed and densely populated regions like the GBA.

5.4.1. The 1962 Xinfengjiang M6.1 earthquake

The epicenter of the 1962 Xinfengjiang *M*6.1 earthquake is near the dam of the Xinfengjiang Reservoir in the western part of Heyuan City and is recognized as one of the largest reservoir-induced earthquakes worldwide (Ding et al., 1983; Gupta, 2002). The FMS shows that this earthquake is a strike-slip faulting event (Fig. 14a). However, which nodal plane represents the seismogenic fault remains a matter of debate. Some researchers proposed that the ENE-trending Heyuan fault (F13) was the rupture plane, given its prominence in the reservoir area and ENE-WSW orientation of the earthquake's isoseismal trend, which aligns with the strike of the Heyuan fault (Shen et al., 1974). On the contrary, more seismological studies, as well as some analyses of fault stress state, argued that the NNW-trending Shijiao-Xingang-Baitian fault was responsible for the earthquake (Fig. 14a) (Wang et al., 1976; Ding et al., 1983; Lin et al., 1988; Qiu and Fenton, 2015). However, the Shijiao-Xingang-Baitian fault consists of several discontinuous small-scale faults (a few hundred meters to a few kilometers long) (Pan and Xiao, 1982; Ding et al., 1983). This raises the question of how these small faults could have generated such a strong earthquake.

Recent seismic tomography results reveal a NW-trending fault beneath the Xinfengjiang Reservoir (Fig. 14a) (He et al., 2018; Dong et al., 2022; Huang et al., 2024). This hidden fault is also evident from the NW-SE preferential orientation of the nodal planes of small normal faulting earthquakes shown in Fig. 14a and related results in He et al. (2018) and Jiang et al. (2022). These findings seem to confirm the existence of the "Shunhe fault" (meaning a fault along the river), which was supposed to be oriented N45°W and was already proposed during the construction of the Xinfengjiang Reservoir (Ding et al., 1983).

The FMSs of the Xinfengjiang Reservoir reflect that the area is subjected to NW-SE compression (Jiang et al., 2022), aligning with the S_H orientations predicted by our model. The NW-trending fault, parallel to S_H, would have a high dilation tendency, as shown in Fig. 9. This fault stress state is likely the fundamental cause for the formation of small normal faulting earthquakes in the Xinfengjiang area.

Recent field investigations have shown that the fault bend connecting the southwestern and northeastern segments of the Heyuan fault between Baitian and Shuangtang is oriented NNW-SSE and is characterized by strike-slip movement; this fault bend coincides exactly with the southern segment of the aforementioned Shijiao-Xingang-Baitian fault (Fig. 14a) (Liu et al., 2017). This finding may provide an important clue for understanding the mechanism of the Xinfengjiang *M*6.1 reservoir-induced earthquake.

We speculate that the seismogenic fault of the *M*6.1 earthquake may be the NNW-SSE-trending fault bend of the Heyuan fault, rather than the Shijiao-Xingang-Baitian fault. One piece of evidence is that earthquakes in this area are mostly concentrated on the fault bend and do not extend northward along the extensive Shijiao-Xingang-Baitian fault (Liu et al., 2017). Moreover, the Heyuan fault is the most prominent large fault in the reservoir area and likely accumulates relatively high strain energy

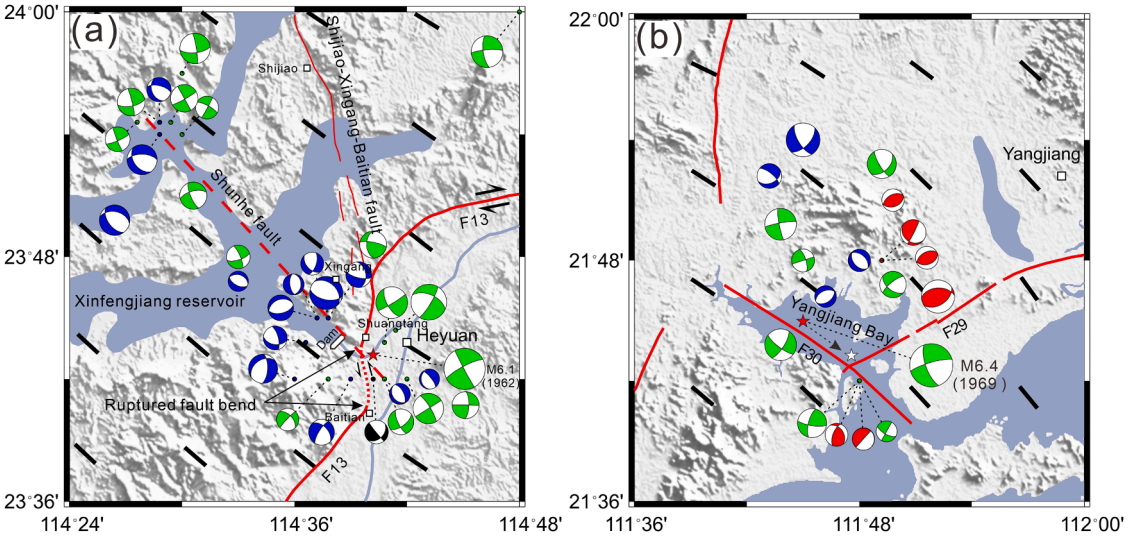

Fig. 14. Distribution of modeled S_H orientations (black bars), faults (red lines), and focal mechanism solutions in (a) the Xinfengjiang reservoir area and (b) the Yangjiang Bay area. In panel (a), the dashed NW-SE line is inferred to be a pre-existing fault, known as the Shunhe fault. The red star represents the location of the 1962 Xinfengjiang *M*6.1 earthquake. The dotted line between Shuangtang and Baitian on the fault bend of the Heyuan fault (F13) is considered the seismogeneric fault of the Xinfengjiang *M*6.1 earthquake. In panel (b), the red star represents the original location of the 1969 Yangjiang *M*6.4 earthquake. Due to the limited number of seismic stations in 1969, the original location may be inaccurate. The exact epicenter of the Yangjiang *M*6.4 earthquake is inferred to be at the intersection of the Pingang fault (F29) and the Yangbianhai fault (F30), as shown by the white star (Li et al., 2024a). The color of focal mechanism solutions is the same as that in Fig. 10.

due to its high angle to the S_H orientation (Liu, 2001) and its relatively significant slip rate of 0.05 mm/a (Li et al., 2024b). The multi-phase extensional activities during the Mesozoic (Li et al., 2014, 2020) likely facilitated the prolongation of the southwestern and northeastern segments of the Heyuan fault, resulting in the formation of the NNW-SSE-trending fault bend that connects these segments through the creation and destruction of relay ramps (e.g., Fossen, 2010, p. 176). This fault bend along the Heyuan fault with significant geometric variation accompanied by the intersection with the NW-trending fault, would be a critical region of stress concentration. After the impoundment of the Xinfengjiang reservoir, water flows downward along the NW-trending permeable faults, increasing the pore pressure and/or decreasing the coefficient of friction at hypocentral depths (e.g., Talwani, 1997), eventually triggering the Xinfengjiang *M*6.1 earthquake on the critically-stressed fault bend.

5.4.2. The 1969 Yangjiang M6.4 earthquake

The 1969 Yangjiang *M*6.4 earthquake occurred in the Yangjiang Bay (also known as Yangbianhai), where the ENE-trending Pinggang fault (F29) intersects the NW-trending Yangbianhai fault (F30) (Fig. 14b). There is a basic consensus that the seismogenic fault of the earthquake is the Pinggang fault (Brantley and Chung, 1991), while the Yangbianhai fault may have experienced a slip during the rupturing of the mainshock (Zhong and Ren, 2003).

The FMSs indicate that the Yangjiang Bay area is mainly subjected to NW-SE compression (Fig. 14b), which is consistent with the regional tectonic regime (Liu, 2001; Zhu et al., 2022) and compares well with our modeled S_H (Fig. 14b). The NW-SE-trending S_H is nearly perpendicular to the ENE-trending Pinggang fault (F29) and parallel to the NW-trending Yangbianhai fault (F30). This relationship between S_H and fault orientations is similar to that of the Xinfengjiang Reservoir area, suggesting a similar explanation for the mechanism of the Yangjiang *M*6.4 earthquake. That is, the crustal stress would produce a higher accumulation of strain energy on the Pinggang fault (F29) by compressing and impart a relatively high permeability to the Yangbianhai fault (F30) by dilating it. Seawater infiltrates down along the permeable Yangbianhai fault to deeper levels, elevating pore pressure and/or decreasing the coefficient of friction, thereby promoting slip of the ENE-trending Pinggang fault to release the accumulated strain energy, ultimately forming the Yangjiang *M*6.4 earthquake. Low seismic shear-wave velocities beneath the intersection area of the Pinggang fault and the Yangbianhai fault are considered to reflect the presence of water-filled fractured rocks created by the intersecting faults (Li et al., 2024a).

Our modeling results also show that the stress level of the Yangjiang Bay area is higher than that of the Xinfengjiang Reservoir area, as indicated by the occurrence of some thrust faulting earthquakes in the Yangjiang Bay area (Fig. 14b) as well as on the Pinggang fault (Kang et al., 2005b; Liu et al., 2005). From a geomechanical perspective, rupturing a fault in a thrust faulting tectonic regime generally requires a higher stress level to overcome the stronger shear resistance on the fault, which is due to the greater normal stress characteristic of this regime.

5.4.3. Implications for seismic hazard

Comparing the Xinfengjiang *M*6.1 and Yangjiang *M*6.4 earthquakes, which are the largest instrumentally recorded events in the study area, we can observe several similarities between them. For example, both earthquakes are related to ENE-trending faults (F13 and F29) that are at high angles to the S_H orientation (Fig. 14). Both events occurred in the intersection area of ENE-trending faults with NW-trending faults and are closely related to water and elevated pore pressures (Fig. 14). The schematic diagram in Fig. 13 can also help to explain the mechanisms behind these strong earthquakes. On the one hand, the ENE-trending faults, which are nearly perpendicular to the S_H orientation, are less likely to rupture and can therefore sustain a higher accumulation of strain energy, leading to stronger earthquakes. On the other hand, fault intersections and fault bends are typical stress concentrators (Gangopadhyay and Talwani, 2003). When water migrates to depth along the permeable NW-trending faults, even a small perturbation in pore pressure and/or the effective coefficient of friction can trigger the critically stressed concentrators to rupture, resulting in a strong earthquake.

This earthquake mechanism is important for the safe development of geothermal resources in the GBA region, as the prospective geothermal systems in the GBA are often located in these stress concentration areas, namely fault intersections and fault bends (Fig. 13). Disturbances in pore pressure or effective friction coefficient caused by water injection and pumping during geothermal development can induce earthquakes (Majer and Peterson, 2007; Megies and Wassermann, 2014). Since ENE-trending faults are important heat-controlling faults in the GBA region, we suggest that special attention should be given to the fault segments which are perpendicular or at a high angle to the S_H orientation, such as F10, F11 and F13 in the eastern part of the study area (Fig. 4). The stress conditions on these segments concern us due to their potential to foster strong earthquakes during geothermal exploitation. More detailed studies on the fault distribution pattern and crustal stress state in geothermal fields are necessary for the safe and sustainable development of geothermal resources in the GBA region.

6. Conclusion

We present a comprehensive 3D geomechanical model of the GBA region to characterize its stress state. The modeled stress field reveals a spatial variation in the S_H orientation, from predominantly NW-SE in the east to near N-S in the west, with a gradual clockwise rotation. This stress field influences fault permeability, with the NW-trending faults inferred to exhibit higher permeabilities than the ENE-/NE-trending faults from a geomechanical perspective. The model also indicates a depth-dependent stress regime with a transition from transpressional in the shallow crust to transtensional at depth. Based on these results, we propose a conceptual model for the genetic mechanism of geothermal resources in the GBA region. We suggest that the intersections of ENE/NE-trending faults with NW-trending faults, as well as fault bends or step-overs along the ENE/NE-trending faults, represent highly prospective areas for geothermal exploration. These areas are also typical stress concentrators. Changes in pore pressure and/or the effective coefficient of friction during geothermal operations have the potential to trigger critically stressed fault segments, potentially leading to significant earthquakes. Therefore, a comprehensive understanding of crustal stress states within geothermal fields is imperative for mitigating seismic risks and ensuring safe and sustainable development of geothermal resources in its future exploitation in the GBA region.

CRediT authorship contribution statement

Xianrui Li: Writing – original draft, Visualization, Validation, Methodology, Investigation, Funding acquisition, Formal analysis, Conceptualization. **Shaopeng Huang:** Writing – review & editing, Supervision, Resources, Project administration, Funding acquisition. **Tobias Hergert:** Writing – review & editing, Methodology. **Andreas Henk:** Writing – review & editing, Methodology. **Danhua Xin:** Writing – review & editing, Funding acquisition.

Declaration of competing interest

The authors declare that they have no known competing financial interests or personal relationships that could have appeared to influence the work reported in this paper.

Acknowledgments

This research is supported by the National Natural Science

Foundation of China (U20A2096, 42204054), the Guangdong Basic and Applied Basic Research Foundation (2023A1515110289) and the Shenzhen Stable Support Plan Program for Higher Education Institutions (20220815084720001). We would like to thank two reviewers and Editor Dr. Sadiq Zarrouk for their insightful comments that helped improved the paper.

Supplementary materials

Supplementary material associated with this article can be found, in the online version, at doi:10.1016/j.geothermics.2025.103253.

Data availability

Data will be made available on request.

References

Ahlers, S., Henk, A., Hergert, T., Reiter, K., Müller, B., Röckel, L., Heidbach, O., Morawietz, S., Scheck-Wenderoth, M., Anikiev, D., 2021. 3D crustal stress state of Western Central Europe according to a data-calibrated geomechanical model. Solid Earth 12, 1777–1799. https://doi.org/10.5194/se-12-1777-2021.

Ahlers, S., Röckel, L., Hergert, T., Reiter, K., Heidbach, O., Henk, A., Müller, B., Morawietz, S., Scheck-Wenderoth, M., Anikiev, D., 2022. The crustal stress field of Germany: a refined prediction. Geothermal Energy 10. https://doi.org/10.1186/s40517-022-00222-6.

Barton, C.A., Zoback, M.D., Moos, D., 1995. Fluid flow along potentially active faults in crystalline rock. Geology. 23, 683. https://doi.org/10.1130/0091-7613(1995)023<0683:FFAPAF>2.3.CO;2.

Blake, K., Davatzes, N., 2011. Crustal Stress Heterogeneity in the Vicinity of Coso Geothermal Field, CA. Thirty-Sixth Workshop on Geothermal Reservoir Engineering. Stanford University.

Brantley, B.J., Chung, W.Y., 1991. Body-wave waveform constraints on the source parameters of the Yangjiang, China, earthquake of July 25, 1969: A devastating earthquake in a stable continental region. Pure Appl. Geophys. 135, 529–543. https://doi.org/10.1007/BF01772404.

Carpenter, B.M., Saffer, D.M., Marone, C., 2015. Frictional properties of the active San Andreas Fault at SAFOD: Implications for fault strength and slip behavior. Journal of Geophysical Research: Solid Earth 120, 5273–5289. https://doi.org/10.1002/2015JB011963.

Chan, L.S., Shen, W., Pubellier, M., 2010. Polyphase rifting of greater Pearl River Delta region (South China): Evidence for possible rapid changes in regional stress configuration. J. Struct. Geol. 32, 746–754. https://doi.org/10.1016/j.jsg.2010.04.015.

Chen, J., Pan, L., Li, Z., Chen, X., 2022. Continental Reworking in the Eastern South China Block and Its Adjacent Areas Revealed by F-J Multimodal Ambient Noise Tomography. Journal of Geophysical Research: Solid Earth 127. https://doi.org/10.1029/2022JB024776 e2022JB024776.

Chen, Q., Fan, T., Li, X., He, S., Zhang, C., Meng, W., 2014. In situ measurements and comprehensive research on the present crustal stress of Northern South China Sea. Chinese Journal of Geophysics 57, 2518–2529. https://doi.org/10.6038/cjg20140813.

Chen, S., Zhang, Y., Tang, D., Tao, S., Pu, Y., Chen, Z., 2024. Present-day stress regime, permeability, and fracture stimulations of coal reservoirs in the Qinshui Basin, northern China. Am. Assoc. Pet. Geol. Bull. 108, 1509–1536. https://doi.org/10.1306/03202422056.

Dávalos-Elizondo, E., Laó-Dávila, D.A., 2023. 3D structural model and slip-dilation tendency analysis of the Chiweta Zone: Geothermal system implications and fault reactivation potential. Journal of African Earth Sciences 198, 104809. https://doi.org/10.1016/j.jafrearsci.2022.104809.

Davatzes, N.C., Hickman, S., Team, E.H., 2006. Stress and Faulting in the Coso Geothermal Field: Update and Recent Results from the East Flank and Coso Wash. Thirty-First Workshop on Geothermal Reservoir Engineering. Stanford University, 13–19.

Ding, Y., Pan, J., Xiao, A., Shen, L., Ma, H., Miao, W., 1983. Tectonic environment of reservoir in the Xinfengjiang reservoir area. Seismology and Geology 5, 63–74.

Dong, H., Lu, T., He, W., Li, Y., Zeng, M., 2016. Quaternary activity of Shawan fault in Pearl River delta. Geology in China 43, 1803–1813. https://doi.org/10.12029/gc20160528.

Dong, N., Yeerzhati, J., Liu, J., 2021. Numerical simulation of fault block movement and stress field characteristics in the Pearl River Delta region. South China Journal of Seismology 41, 100–109. https://doi.org/10.13512/j.hndz.2021.03.14.

Dong, S., Li, J., Cawood, P.A., Gao, R., Zhang, Y., Xin, Y., 2020. Mantle influx compensates crustal thinning beneath the Cathaysia Block, South China: Evidence from SINOPROBE reflection profiling. Earth. Planet. Sci. Lett. 544, 116360. https://doi.org/10.1016/j.epsl.2020.116360.

Dong, S., Li, L., Zhao, L., Shen, X., Wang, W., Huang, H., Peng, B., Xu, X., Gao, R., 2022. Seismic Evidence for Fluid-Driven Pore Pressure Increase and Its Links With Induced Seismicity in the Xinfengjiang Reservoir, South China. Journal of Geophysical Research: Solid Earth 127. https://doi.org/10.1029/2021JB023548 e2021JB023548.

Duwiquet, H., Magri, F., Lopez, S., Guillon, T., Arbaret, L., Bellanger, M., Guillou-Frottier, L., 2022. Tectonic Regime as a Control Factor for Crustal Fault Zone (CFZ) Geothermal Reservoir in an Amagmatic System: A 3D Dynamic Numerical Modeling Approach. Natural Resources Research 31, 3155–3172. https://doi.org/10.1007/s11053-022-10116-w.

Evans, J.P., Forster, C.B., Goddard, J.V., 1997. Permeability of fault-related rocks, and implications for hydraulic structure of fault zones. J. Struct. Geol. 19, 1393–1404. https://doi.org/10.1016/S0191-8141(97)00057-6.

Evans, K.F., Zappone, A., Kraft, T., Deichmann, N., Moia, F., 2012. A survey of the induced seismic responses to fluid injection in geothermal and CO2 reservoirs in Europe. Geothermics. 41, 30–54. https://doi.org/10.1016/j.geothermics.2011.08.002.

Fan, Y., Li, H., Zhang, J., Wang, Q., Ren, T., Zhang, M., Huang, S., Qin, X., 2022. Research on the in-situ stress state and the geothermal-controlling structure of the Huangshadong Geothermal Field in the Southeast Coast of China. Chinese Journal of Geophysics 65, 3944–3961. https://doi.org/10.6038/cjg2022P0892.

Fang, C., 2012. Distribution of hot springs in Heyuan City and their development prospects. Sichuan Building Materials 38, 59–60.

Feng, C., Chen, Q., Tan, C., Wu, M., Qin, X., 2013. In-situ stress measurement and its application to Guangdong nuclear power stations. Rock and Soil Mechanics 34, 1745–1752. https://doi.org/10.16285/j.rsm.2013.06.020.

Ferrill, D.A., Morris, A.P., 2003. Dilational normal faults. J. Struct. Geol. 25, 183–196. https://doi.org/10.1016/S0191-8141(02)00029-9.

Ferrill, D.A., Winterle, J., Wittmeyer, G., Sims, D., Colton, S., Armstrong, A., Morris, A.P., 1999. Stressed Rock Strains Groundwater at Yucca Mountain. Nevada. GSA TODAY 1–8.

Fossen, H., 2010. Structural Geology. Cambridge University Press, New York.

Gangopadhyay, A., Talwani, P., 2003. Symptomatic Features of Intraplate Earthquakes. Seismological Research Letters 74, 863–883. https://doi.org/10.1785/gssrl.74.6.863.

GBGM, 1988. Regional Geology of Guangdong Province. Geology Press, Beijing.

Guo, L., Gao, R., Shi, L., Huang, Z., Ma, Y., 2019. Crustal thickness and Poisson's ratios of South China revealed from joint inversion of receiver function and gravity data. Earth. Planet. Sci. Lett. 510, 142–152. https://doi.org/10.1016/j.epsl.2018.12.039.

Gupta, H.K., 2002. A review of recent studies of triggered earthquakes by artificial water reservoirs with special emphasis on earthquakes in Koyna. India. Earth-Science Reviews 58, 279–310. https://doi.org/10.1016/S0012-8252(02)00063-6.

Hardebeck, J.L., Michael, A.J., 2006. Damped regional-scale stress inversions: Methodology and examples for southern California and the Coalinga aftershock sequence. J. Geophys. Res. 111, B11310. https://doi.org/10.1029/2005JB004144.

He, J., Lu, S., 2007. Lower friction of the Xianshuihe-Xiaojiang fault system and its effect on active deformation around the south-eastern Tibetan margin. Terra Nova 19, 204–210. https://doi.org/10.1111/j.1365-3121.2007.00735.x.

He, L., Sun, X., Yang, H., Qin, J., Shen, Y., Ye, X., 2018. Upper Crustal Structure and Earthquake Mechanism in the Xinfengjiang Water Reservoir, Guangdong, China. Journal of Geophysical Research: Solid Earth 123, 3799–3813. https://doi.org/10.1029/2017JB015404.

Heidbach, O., Rajabi, M., Cui, X., Fuchs, K., Müller, B., Reinecker, J., Reiter, K., Tingay, M., Wenzel, F., Xie, F., Ziegler, M.O., Zoback, M.L., Zoback, M., 2018. The World Stress Map database release 2016: Crustal stress pattern across scales. Tectonophysics. 744, 484–498. https://doi.org/10.1016/j.tecto.2018.07.007.

Heidbach, O., Tingay, M., Barth, A., Reinecker, J., Kurfeß, D., Müller, B., 2010. Global crustal stress pattern based on the World Stress Map database release 2008. Tectonophysics. 482, 3–15. https://doi.org/10.1016/j.tecto.2009.07.023.

Henk, A., Nemčok, M., 2008. Stress and fracture prediction in inverted half-graben structures. J. Struct. Geol. 30, 81–97. https://doi.org/10.1016/j.jsg.2007.10.006.

Hergert, T., Heidbach, O., 2011. Geomechanical model of the Marmara Sea region—II. 3-D contemporary background stress field. Geophys. J. Int. 185, 1090–1102. https://doi.org/10.1111/j.1365-246X.2011.04992.x.

Hergert, T., Heidbach, O., 2010. Slip-rate variability and distributed deformation in the Marmara Sea fault system. Nat. Geosci. 3, 132–135. https://doi.org/10.1038/ngeo739.

Hergert, T., Heidbach, O., Reiter, K., Giger, S.B., Marschall, P., 2015. Stress field sensitivity analysis in a sedimentary sequence of the Alpine foreland, northern Switzerland. Solid Earth 6, 533–552. https://doi.org/10.5194/se-6-533-2015.

Huang, H., Zheng, J., 2001. Research on kinematic characteristics of Wuchuan-Sihui fault zone. Uranium Geology 17, 34–43.

Huang, R., Sun, X., Zhang, P., Deng, Y., 2024. Seismicity Migration and the Upper Crustal Structure in the Xinfengjiang Reservoir. Seismological Research Letters. https://doi.org/10.1785/0220230369.

Huang, S., 2012. Geothermal energy in China. Nat. Clim. Chang. 2, 557–560. https://doi.org/10.1038/nclimate1598.

Jiang, G., Hu, S., Shi, Y., Zhang, C., Wang, Z., Hu, D., 2019. Terrestrial heat flow of continental China: Updated dataset and tectonic implications. Tectonophysics. 753, 36–48. https://doi.org/10.1016/j.tecto.2019.01.006.

Jiang, X., Lin, Q., Gong, X., Yang, X., 2022. Earthquake focal mechanism solutions and spatio-temporal variations of tectonic stress field in Xinfengjiang reservoir since 2012. Earthquake 42, 64–80.

Jolie, E., Klinkmueller, M., Moeck, I., Bruhn, D., 2016. Linking gas fluxes at Earth's surface with fracture zones in an active geothermal field. Geology. 44, 187–190. https://doi.org/10.1130/G37412.1.

Jolie, E., Moeck, I., Faulds, J.E., 2015. Quantitative structural–geological exploration of fault-controlled geothermal systems—A case study from the Basin-and-Range Province, Nevada (USA). Geothermics. 54, 54–67. https://doi.org/10.1016/j.geothermics.2014.10.003.

Kang, Y., Yang, X., Chen, X., Chen, G., Zheng, S., 2008. Sress field in Guangdong and its adjacent area. Acta Seismologica Sinica 30, 59–66.
Kang, Y., Yang, X., Lv, J., Chen, X., Chen, G., 2005a. Characteristics of focal mechanism in the Guangdong and its adjacent areas. Earthquake Research in China 21, 320–331.
Kang, Y., Yang, X., Lv, J., Ye, F., 2005b. Analysis on the source parameters of Yangjiang earthquake with Ms4.9 in 2004. Earthquake 25, 109–114.
Kim, K.H., Ree, J.H., Kim, Y., Kim, S., Kang, S.Y., Seo, W., 2018. Assessing whether the 2017 M_w 5.4 Pohang earthquake in South Korea was an induced event. Science 360, 1007–1009. https://doi.org/10.1126/science.aat6081.
Kranzz, R.L., Frankel, A.D., Engelder, T., Scholz, C.H., 1979. The permeability of whole and jointed Barre Granite. International Journal of Rock Mechanics and Mining Sciences & Geomechanics Abstracts 16, 225–234. https://doi.org/10.1016/0148-9062(79)91197-5.
Kuo, L.W., Li, H., Smith, S.A.F., Toro, G.D., Suppe, J., Song, S.R., Nielsen, S., Sheu, H.S., Si, J., 2014. Gouge graphitization and dynamic fault weakening during the 2008 Mw 7.9 Wenchuan earthquake. Geology 42, 47–50. https://doi.org/10.1130/G34862.1.
Lai, C.Y., Wong, L.N.Y., Wallace, M., 2019. Review and assessment of In-situ rock stress in Hong Kong for territory-wide geological domains and depth profiling. Eng. Geol. 248, 267–282. https://doi.org/10.1016/j.enggeo.2018.11.008.
Laske, G., Masters, G., Ma, Z., Pasyanos, M., 2013. Update on CRUST1. 0—A 1-degree global model of Earth's crust. Geophysical Research Abstracts. EGU General Assembly Vienna, Austria 2658.
Li, H., Xue, L., Brodsky, E.E., Mori, J.J., Fulton, P.M., Wang, H., Kano, Y., Yun, K., Harris, R.N., Gong, Z., Li, C., Si, J., Sun, Z., Pei, J., Zheng, Y., Xu, Z., 2015. Long-term temperature records following the Mw 7.9 Wenchuan (China) earthquake are consistent with low friction. Geology. 43, 163–166. https://doi.org/10.1130/G35515.1.
Li, J., Cawood, P.A., Ratschbacher, L., Zhang, Y., Dong, S., Xin, Y., Yang, H., Zhang, P., 2020. Building Southeast China in the late Mesozoic: Insights from alternating episodes of shortening and extension along the Lianhuashan fault zone. Earth. Sci. Rev. 201, 103056. https://doi.org/10.1016/j.earscirev.2019.103056.
Li, J., Zhang, Y., Dong, S., Johnston, S.T., 2014. Cretaceous tectonic evolution of South China: A preliminary synthesis. Earth. Sci. Rev. 134, 98–136. https://doi.org/10.1016/j.earscirev.2014.03.008.
Li, L., Zhang, J., Shen, X., Wang, X., He, J., Zhao, L., Deng, Z., Gao, R., 2024a. Seismological Constraints on the Causes of Intraplate Earthquakes in Yangjiang Region, South China. Journal of Geophysical Research: Solid Earth 129, e2023JB027715. https://doi.org/10.1029/2023JB027715.
Li, X., Gao, K., Feng, Y., Zhang, C., 2022a. 3D geomechanical modeling of the Xianshuihe fault zone, SE Tibetan Plateau: Implications for seismic hazard assessment. Tectonophysics. 839, 229546. https://doi.org/10.1016/j.tecto.2022.229546.
Li, X., Hergert, T., Henk, A., Zeng, Z., 2022b. Contemporary background stress field in the eastern Tibetan Plateau: Insights from 3D geomechanical modeling. Tectonophysics. 822, 229177. https://doi.org/10.1016/j.tecto.2021.229177.
Li, X., Hergert, T., Henk, A., Zeng, Z., 2021. Contemporary kinematics in the eastern Tibetan Plateau: Insights from 3D geomechanical modeling. Tectonophysics. 819, 229109. https://doi.org/10.1016/j.tecto.2021.229109.
Li, X., Huang, S., Hergert, T., Henk, A., Du, Q., 2024b. Contemporary crustal kinematics in the Guangdong-Hong Kong-Macao Greater Bay Area, SE China: Implications for the geothermal resource exploration. J. Asian Earth. Sci. 263, 106041. https://doi.org/10.1016/j.jseaes.2024.106041.
Li, Y., Luo, J., Tian, J., Cheng, Y., Pang, Z., Huang, T., Fan, Y., 2023. Formation of the hydrothermal system from granite reservoir for power generation in igneous rock areas of South China. Geothermics. 110, 102673. https://doi.org/10.1016/j.geothermics.2023.102673.
Lin, B., Dong, D., Lin, J., Hu, X., 1988. A study on the inversion of rupture process by using the compound model method. Acta Seismologica Sinica 10, 337–351.
Lin, W., Wang, G., Gan, H., 2024. Differential crustal thermal structure and geothermal significance in the igneous region of southeastern China. Acta Geologica Sinica 98, 544–557. https://doi.org/10.19762/j.cnki.dizhixuebao.2023027.
Lin, W., Wang, G., Gan, H., Wang, A., Yue, G., Long, X., 2022. Heat generation and accumulation for hot dry rock resources in the igneous rock distribution areas of southeastern China. Lithosphere 2021, 2039112. https://doi.org/10.2113/2022/2039112.
Liu, L., 2001. Stable Continental Region Earthquakes in South China. Pure Appl. Geophys. 158, 1583–1611. https://doi.org/10.1007/PL00001235.
Liu, L., Zoback, M.D., 1992. The effect of topography on the state of stress in the crust: Application to the site of the Cajon Pass Scientific Drilling Project. J. Geophys. Res. 97, 5095. https://doi.org/10.1029/91JB01355.
Liu, T., Qin, N., Chen, Y., 2005. Seismicity characteristics, influence field and emergency countermeasures of the Guangdong Yangjiang Ms4.9 earthquake. Seismologcial and Geomagnetic Observation and Research 26, 33–41.
Liu, T., Shao, Y., Yang, X., Tan, Z., Ding, Y., 2017. Determination of the NW-trending faults in Xinfengjiang Reservoir dam by using high-precision small earthquakes data. Acta Seismologica Sinica 39, 23–33.
Lockner, D.A., Morrow, C., Moore, D., Hickman, S., 2011. Low strength of deep San Andreas fault gouge from SAFOD core. Nature 472, 82–85. https://doi.org/10.1038/nature09927.
Lu, R., Jiang, C., He, D., Wang, W., Guo, Z., Zhang, W., Tao, W., Yang, X., Lai, G., Zhan, Y., Liu, G., Xu, F., Sun, X., 2024. Seismogenic fault of the 2021 Ms 6.0 Luxian induced earthquake in the Sichuan Basin, China constrained by high-resolution seismic reflection and dense seismic array. J. Struct. Geol. 179, 105050. https://doi.org/10.1016/j.jsg.2024.105050.
Lund, B., Townend, J., 2007. Calculating horizontal stress orientations with full or partial knowledge of the tectonic stress tensor. Geophys. J. Int. 170, 1328–1335. https://doi.org/10.1111/j.1365-246X.2007.03468.x.
Luo, J., Li, Y., Tian, J., Cheng, Y., Pang, Z., Gong, Y., 2022. Geochemistry of geothermal fluid with implications on circulation and evolution in Fengshun-Tangkeng geothermal field, South China. Geothermics. 100, 102323. https://doi.org/10.1016/j.geothermics.2021.102323.
Lv, Z., Huang, H., Ye, X., Lü, J., Xiong, C., 2022. High-Resolution Crustal Shear-Wave Velocity Structure in the Pearl River Delta, South China. Seismological Research Letters 93, 338–350. https://doi.org/10.1785/0220210116.
Lv, Z., Qiu, X., Lv, J., Huang, H., Ye, X., Wang, S., Wang, L., Wang, X., 2020. Crustal structure beneath the east side of Pearl River Estuary from onshore-offshore seismic experiment. Int. Geol. Rev. 62, 1057–1069. https://doi.org/10.1080/00206814.2018.1553114.
Majer, E.L., Peterson, J.E., 2007. The impact of injection on seismicity at The Geysers, California Geothermal Field. International Journal of Rock Mechanics and Mining Sciences 44, 1079–1090. https://doi.org/10.1016/j.ijrmms.2007.07.023.
Mao, X., Wang, H., Feng, L., 2018. Impact of additional dead carbon on the circulation estimation of thermal springs exposed from deep-seated faults in the Dongguan basin, southern China. Journal of Volcanology and Geothermal Research 361, 1–11. https://doi.org/10.1016/j.jvolgeores.2018.08.002.
Mardia, K.V., Jupp, P.E., 2000. Directional Statistics. John Wiley & Sons, New York.
Martínez-Garzón, P., Kwiatek, G., Ickrath, M., Bohnhoff, M., 2014. MSATSI: A MATLAB package for stress inversion combining solid classic methodology, a new simplified user-handling, and a visualization tool. Seismological Research Letters 85, 896–904. https://doi.org/10.1785/0220130189.
Megies, T., Wassermann, J., 2014. Microseismicity observed at a non-pressure-stimulated geothermal power plant. Geothermics. Analysis of Induced Seismicity in Geothermal Operations 52, 36–49. https://doi.org/10.1016/j.geothermics.2014.01.002.
Moeck, I., Schandelmeier, H., Holl, H.G., 2009. The stress regime in a Rotliegend reservoir of the Northeast German Basin. International Journal of Earth Sciences 98, 1643–1654. https://doi.org/10.1007/s00531-008-0316-1.
Moeck, I.S., 2014. Catalog of geothermal play types based on geologic controls. Renewable and Sustainable Energy Reviews 37, 867–882. https://doi.org/10.1016/j.rser.2014.05.032.
Moein, M.J., Langenbruch, C., Schultz, R., Grigoli, F., Ellsworth, W.L., Wang, R., Rinaldi, A.P., Shapiro, S., 2023. The physical mechanisms of induced earthquakes. Nature Reviews Earth & Environment 4, 847–863. https://doi.org/10.1038/s43017-023-00497-8.
Morris, A., Ferrill, D.A., Brent Henderson, D.B., 1996. Slip-tendency analysis and fault reactivation. Geology. 24, 275. https://doi.org/10.1130/0091-7613(1996)024<0275:STAAFR>2.3.CO;2.
Morrow, C., Lockner, D., Hickman, S., Rusanov, M., Röckel, T., 1994. Effects of lithology and depth on the permeability of core samples from the Kola and KTB drill holes. Journal of Geophysical Research: Solid Earth 99, 7263–7274. https://doi.org/10.1029/93JB03458.
Pan, J., Xiao, A., 1982. The preliminary study of seismic structures and their characteristic activity in Xinfengjiang reservoir area. Seismology and Geology 4, 53–58.
Qiu, X., Fenton, C., 2015. Factors Controlling the Occurrence of Reservoir-Induced Seismicity. In: Lollino, G., Giordan, D., Thuro, K., Carranza-Torres, C., Wu, F., Marinos, P., Delgado, C. (Eds.), Engineering Geology for Society and Territory - Volume 6. Springer International Publishing, Cham, 567–570. 10.1007/978-3-319-09060-3_102.
Reiter, K., Heidbach, O., 2014. 3-D geomechanical–numerical model of the contemporary crustal stress state in the Alberta Basin (Canada). Solid Earth 5, 1123–1149. https://doi.org/10.5194/se-5-1123-2014.
Shen, C., Chen, H., Zhang, C., Huang, L., Li, Z., Yang, Z., Wang, D., 1974. Xinfengjiang reservoir earthquake and its impact on the dam. Science China 2, 184–205.
Sheorey, P.R., 1994. A theory for In Situ stresses in isotropic and transverseley isotropic rock. International Journal of Rock Mechanics and Mining Sciences & Geomechanics Abstracts 31, 23–34. https://doi.org/10.1016/0148-9062(94)92312-4.
Shu, L., Yao, J., Wang, B., Faure, M., Charvet, J., Chen, Y., 2021. Neoproterozoic plate tectonic process and Phanerozoic geodynamic evolution of the South China Block. Earth. Sci. Rev. 216, 103596. https://doi.org/10.1016/j.earscirev.2021.103596.
Siler, D.L., Faulds, J.E., Hinz, N.H., Dering, G.M., Edwards, J.H., Mayhew, B., 2019. Three-dimensional geologic mapping to assess geothermal potential: examples from Nevada and Oregon. Geothermal Energy 7, 2. https://doi.org/10.1186/s40517-018-0117-0.
Siler, D.L., Hinz, N.H., Faulds, J.E., 2018. Stress concentrations at structural discontinuities in active fault zones in the western United States: Implications for permeability and fluid flow in geothermal fields. GSA Bulletin 130, 1273–1288. https://doi.org/10.1130/B31729.1.
Simpson, R.W., 1997. Quantifying Anderson's fault types. J. Geophys. Res. 102, 17909–17919. https://doi.org/10.1029/97JB01274.
Simpson, R.W., Reasenberg, P.A., 1994. The Lorna Prieta, California, Earthquake of October 17, 1989-Tectonic Processes and Models. U.S. Geological Survey, pp. F55–F89. Professional Paper 1550-F.
Stromeyer, D., Heidbach, O., Ziegler, M., 2020. Tecplot 360 Add-on GeoStress v2. 0. GFZ Data Services.
Talwani, P., 1997. On the Nature of Reservoir-induced Seismicity. Pure Appl. Geophys. 150, 473–492. https://doi.org/10.1007/s000240050089.
Tang, X., Hu, S., Zhang, G., Yang, S., Shen, H., Rao, S., Li, W., 2014. Characteristic of surface heat flow in the Pearl River Mouth Basin and its relationship with thermal lithosphere thickness. Chin. J. Geophys. 57, 1857–1867. https://doi.org/10.6038/cjg20140617.
Tannock, L., Herwegh, M., Berger, A., Liu, J., Lanari, P., Regenauer-Lieb, K., 2020a. Microstructural analyses of a giant quartz reef in south China reveal episodic brittle-

ductile fluid transfer. J. Struct. Geol. 130, 103911. https://doi.org/10.1016/j.jsg.2019.103911.
Tannock, L., Herwegh, M., Berger, A., Liu, J., Regenauer-Lieb, K., 2020b. The effects of a tectonic stress regime change on crustal-scale fluid flow at the Heyuan geothermal fault system, South China. Tectonophysics. 781, 228399. https://doi.org/10.1016/j.tecto.2020.228399.
Tian, J., Stefánsson, A., Li, Y., Li, L., Xing, L., Li, Z., Li, Y., Zhou, X., 2023. Geochemistry of thermal fluids and the genesis of granite-hosted Huangshadong geothermal system, Southeast China. Geothermics. 109, 102647. https://doi.org/10.1016/j.geothermics.2023.102647.
Wang, M., Shen, Z., 2020. Present-Day Crustal Deformation of Continental China Derived From GPS and Its Tectonic Implications. Journal of Geophysical Research: Solid Earth 125, e2019JB018774. https://doi.org/10.1029/2019JB018774.
Wang, M., Yang, M., Hu, Y., Li, Z., Chen, Y., Jin, Y., 1976. Mechanism of the reservoir impounding earthquakes at Xinfengjiang and a preliminary endeavour to discuss their cause. Chinese Journal of Geophysics 19, 1–17.
Wei, B., 2001. Characteristics of Earthquake Activity Along the Southeast Coast. Seismological Press, Beijing.
Wei, Z., Huang, S., Wang, C., 2024a. Geochemistry and sources of boron and strontium of geothermal waters from the Pearl River Delta region, South China: Implications for water-rock interactions. J. Geochem. Explor. 262, 107492. https://doi.org/10.1016/j.gexplo.2024.107492.
Wei, Z., Huang, S., Xu, J., Yuan, C., Zhang, M., Wang, C., 2024b. Geochemical evolution of geothermal waters in the Pearl River Delta region, South China: Insights from water chemistry and isotope geochemistry. Journal of Hydrology: Regional Studies 51, 101670. https://doi.org/10.1016/j.ejrh.2024.101670.
Wei, Z., Huang, S., Xu, J., Yuan, C., Zhang, M., Wang, C., 2024c. Geochemical evolution of geothermal waters in the Pearl River Delta region, South China: Insights from water chemistry and isotope geochemistry. Journal of Hydrology: Regional Studies 51, 101670. https://doi.org/10.1016/j.ejrh.2024.101670.
Wen, Z., Qang, Z., Yang, M., 2001. The simulation of the modern geotectonic stress field of Guangdong area. South China Journal of Seismology 21, 29–36.
Xia, S., Lin, J., Cao, J., 2022. Seismicity and seismogenic structure in the northern coastal area of the South China Sea. Geotectonica et Metallogenia 46, 455–470.
Xu, J., Huang, S., Wei, Z., Li, Y., 2023. Spatial characteristics of geothermal anomalies in the Guangdong-Hong Kong-Macao Greater Bay Area based on GIS. Journal of Shenzhen University Science and Engineering 40, 588–598.
Xu, X., Han, Z., Yang, X., 2016. Seismotectonic Map of China and Its Adjacent Areas. Seismological Press, Beijing.
Yao, Z., Chen, Z., 1990. Geological assessment of geothermal potential for regional development in southeast coast of China. Bulletin Institute of Hydrogeology and Engineering Geology CAGS 6, 47–80.
Ye, X., Huang, Y., Liu, J., 2016. 3D P-wave velocity structure and active tectonics in the Xinfengjiang area of Guangdong. Earthquake Research in China 32, 465–476.
Yu, S.B., Kuo, L.C., Punongbayan, R.S., Ramos, E.G., 1999. GPS observation of crustal deformation in the Taiwan-Luzon Region. Geophys. Res. Lett. 26, 923–926. https://doi.org/10.1029/1999GL900148.
Yu, Z., Zhang, K., Liang, H., Li, Z., 2016. Late quaternary tectonic movements in the Pearl River Delta, China, Revealed from stratigraphic profiles. Tropical Geography 36, 334–342.
Yuan, J., Xu, F., Zheng, T., 2022. The genesis of saline geothermal groundwater in the coastal area of Guangdong Province: Insight from hydrochemical and isotopic analysis. J. Hydrol. 605, 127345. https://doi.org/10.1016/j.jhydrol.2021.127345.
Zhang, C., Li, B., Li, H., He, M., Gan, H., Wang, G., Fan, Y., 2023. Stress estimation in a 3 km-deep geothermal borehole: a snapshot of stress state in Southern Cathaysia block, China. Tectonophysics 864, 230031. https://doi.org/10.1016/j.tecto.2023.230031.
Zhang, L., He, C., 2013. Frictional properties of natural gouges from Longmenshan fault zone ruptured during the Wenchuan Mw7.9 earthquake. Tectonophysics. 594, 149–164. https://doi.org/10.1016/j.tecto.2013.03.030.
Zhang, X., Ye, X., Lv, J., Sun, J., Wang, X., 2018. Crustal structure revealed by a deep seismic sounding profile of Baijing-Gaoming-Jinwan in the Pearl River Delta. Journal of Ocean University of China 17, 186–194. https://doi.org/10.1007/s11802-018-3489-7.
Zhong, J., Zhou, D., 1990. A Preliminary study of the relationship between the distribution of hot springs and the activity of earthquakes along South China Coast. South China Journal of Seismology 10, 22–29.
Zhong, Y., Ren, Z., 2003. Study on seismogenic tectonic of Yangjiang M6.4 earthquake. Journal of Geodesy and Geodynamics 23, 92–98.
Zhou, X., Li, W., 2000. Origin of Late Mesozoic igneous rocks in Southeastern China: implications for lithosphere subduction and underplating of mafic magmas. Tectonophysics. 326, 269–287. https://doi.org/10.1016/S0040-1951(00)00120-7.
Zhou, X., Sun, T., Shen, W., Shu, L., Niu, Y., 2006. Petrogenesis of Mesozoic granitoids and volcanic rocks in South China: a response to tectonic evolution. Episodes Journal of International Geoscience 29, 26–33. https://doi.org/10.18814/epiiugs/2006/v29i1/004.
Zhou, Z.M., Ma, C.Q., Qi, S.H., Xi, Y.F., Liu, W., 2020. Late Mesozoic high-heat-producing (HHP) and high-temperature geothermal reservoir granitoids: The most significant geothermal mechanism in South China. Lithos. 366–367, 105568. https://doi.org/10.1016/j.lithos.2020.105568.
Zhu, J., Li, S., Chen, X., Li, J., Li, Y., Xing, H., Jia, Y., 2022. Large intraplate earthquakes and static stress changes in the South China coastal region. Gondwana Research 102, 46–59. https://doi.org/10.1016/j.gr.2020.03.004.
Zhu, L., Ben-Zion, Y., 2013. Parametrization of general seismic potency and moment tensors for source inversion of seismic waveform data. Geophys. J. Int. 194, 839–843. https://doi.org/10.1093/gji/ggt137.
Zoback, M.L., 1992. First- and second-order patterns of stress in the lithosphere: The World Stress Map Project. J. Geophys. Res. 97, 11703. https://doi.org/10.1029/92JB00132.